Copyright

by

Max Fabian Riedel

2006

Elastic Slowing of Supersonic Beams

by

Max Fabian Riedel

Thesis

Presented to the Faculty of the Graduate School of

The University of Texas at Austin

in Partial Fulfillment

of the Requirements

for the Degree of

Master of Arts

The University of Texas at Austin

December 2006

Elastic Slowing of Supersonic Beams

Approved by
Supervising Committee:

_____

_____

For my parents.

Thank you for your love and support.

Acknowledgments

First of all, I would like to thank my supervisor, Prof. Mark Raizen. Mark, you allowed me great freedom in my work and put a lot of trust in me. Nevertheless, you were always there with good advice and great ideas when I needed you. I am very proud that I was given the opportunity to work in your group. Thank you for supporting me during my time in Austin and beyond.

I am equally thankful to my fellow group members and friends Adam Libson, Dr. Ed Narevicius and Christian Parthey. Everything we accomplished during the last one and a half years was a group effort and they are the main reason I am writing this thesis using the pronoun "we".

Adam, although you sometimes "unnerved" us with your constant fear of leaks or fatal rotor destruction, I wouldn't have wanted to work with anybody else than you on this project. You often foresaw problems we would have easily overlooked and solved them as well as many others in your intelligent and practical manner. You are a dear friend to me and I wish you the best for your future graduate studies, your career as a physicist, which will, considering your love for the subject, surely be a great one, and life beyond physics.

Ed, you often asked the questions that made me concentrate on the important aspects of a problem, made me rethink our previous approach or simply made the problem vanish. By making me see things from a different perspective, you were a mentor without ever acting superior (after all, "you are the postdoc"). I thank you

for working with me, for bringing some sereneness in our lab, for advising me on my plans for the future and for being my friend. I wish you success in your professional life and you and your family great happiness in your private life. “Thank y’all!”

Christian, you came in our lab when we were just starting to build the experiment, so you were thrown in at the deep end. I was amazed how quickly you became an integral part of the group and now, I can’t imagine the Raizen lab without you. Sure, your intelligence and determination helped, but I think the true reason for this is that we all instantly liked you and that you have by now become a good friend. I wish you a fun and successful year in Austin and the best for your future plans.

Prof. Uzi Even is the inventor of the pulsed supersonic valve that is a key component of our experiment and visited us for two months during the fall semester 2006. He helped and guided us from setting up the first parts in the lab to the successful detection of the slow beam. Uzi, I can’t thank you enough for being there during this time. Without your immense experience and incredible intuition for experimental physics we would have not gotten where we are now in such a short amount of time. Besides work, I very much enjoyed the long conversations about politics, culture and life we had and hope we will stay in contact.

Isaac Chavez is an undergraduate student who built the gas mixing and distribution system and will join the experiment as a grad student in the summer of 2007. Isaac, I thank you for your help and wish you a successful graduation and good luck as a grad student.

I would like to thank all of the above and the remaining members of the Raizen lab, Travis Bannerman, Chih-Sung Chuu, Kevin Henderson, Hrishikesh Kelkar, Tongcang Li, David Medellin, Julia Narevicius, Gabriel Price and Kirsten Viering for the great atmosphere in which I had the privilege to work.

Many thanks to Prof. Greg Sitz for advising us on questions about surface science during the experiment and for being the reader of this thesis.

I would like to thank Alexander Khajetoorians for helping us getting started with the silicon passivation. His experience and advice saved us many hours of work under the fume hood.

The machine shop did a terrific job in building the parts we needed, sometimes after hours or even on the weekend. They always had very helpful suggestions on how to improve parts to make them more efficient or precise. I would like to thank especially Allan Schroeder, Herb Boehl, George Sandefur, and Jack Clifford.

Many thanks to Olga Vera and Elena Simmons for taking care of our paperwork and any other bureaucracy we had to face and for being patient with us when we forgot to turn in our PO cover sheets.

Many thanks also to Mike Tiner and Dr. Bill Lackowsky from the Center for Nano and Molecular Science and Technology here at UT for their help with the AFM and dicing saw.

The Center for Electromechanics advised us on rotor and spindle construction. Many thanks to Dr. Robert Hebner, Jim Weldon and Brian Murphy for this.

Sincere thanks to Prof. Manfred Fink in Austin and Prof. Manfred Böhm and Prof. Hansheinrich Langhoff in Würzburg for organizing the exchange between the two universities. It has been a wonderful experience and I hope that many more students will have the opportunity to take part in this program in the future. For funding this exchange, I would like to thank the DAAD.

Last but not least, I am very grateful for my friends here in Austin, especially Kirsten, Hannah, Adam, Christian, and Thomas.

Max Fabian Riedel

The University of Texas at Austin
December 2006

Elastic Slowing of Supersonic Beams

Max Fabian Riedel, M.A.
The University of Texas at Austin, 2006

Supervisor: Mark G. Raizen

In this thesis we describe a new method of producing an intense, cold beam of slow noble gas atoms. A beam produced by a pulsed cryogenic supersonic nozzle is reflected from a single crystal atom mirror mounted on the tip of a spinning rotor. Simulations show that fluxes of 10^{11} He atoms per second at velocities of 50m/s and temperatures of less than $20\mu K$ in the longitudinal direction are feasible. We describe in detail the apparatus built in our laboratory. We are able to tune the speed of a He-Ne mixture from 265m/s to 510m/s while maintaining a cold, monochromatic beam. We plan to reduce the speed of the reflected beam further to under 100m/s in the future by simple modifications of our system.

Contents

Acknowledgments **v**

Abstract **ix**

Chapter 1 Introduction **1**

Chapter 2 The beam slowing apparatus **4**

2.1 High intensity cryogenic pulsed supersonic nozzle 4

2.1.1 Gas flow in the supersonic regime 6

2.2 The rotor as a beam slower 10

2.3 Atomic mirrors and lenses 11

2.4 Noble gas atom detector 14

Chapter 3 Simulation of the beam **15**

3.1 Simulated system and simulation method 15

3.2 Results of the simulation 17

3.2.1 Expected flux 17

3.2.2 Influence of the focusing mirror 18

3.2.3 Energy resolution of the beam 19

Chapter 4 Designing and building the vacuum chamber and rotor assembly **21**

4.1 The vacuum chamber . . . 23
4.2 The rotor and spindle . . . 26
4.2.1 Balancing the rotor . . . 31
4.3 Atomic mirrors and mirror holders . . . 36
4.3.1 Atomic mirrors . . . 36
4.3.2 Cleaning and etching procedure of the atom mirrors . . . 37
4.3.3 Mirror holder and clamp . . . 40
4.4 Atom detector . . . 42
4.4.1 Beam broadening in the RGAs . . . 45

Chapter 5 Experimental results **48**
5.1 The direct supersonic beam . . . 48
5.2 The slowed beam . . . 52
5.3 Crystal life time . . . 55

Chapter 6 Future work **57**
6.1 Improving the performance of the apparatus . . . 57
6.2 Velocity dispersion compensation piston . . . 58
6.3 Atom beam splitter . . . 59
6.4 Proposed uses of the beam . . . 60
6.4.1 Characterizing the atom surface potential . . . 60
6.4.2 Atom interferometer . . . 61
6.5 The magnetic slower . . . 62

Chapter 7 Conclusions **65**

Bibliography **67**

Vita **70**

Chapter 1

Introduction

Atom optics has been a rapidly growing field in recent years due to the enormous potential for precision measurements as well as fundamental physics [1]. The main focus to date has been on methods of laser cooling and trapping to control atomic translational motion, combined with the control of the internal atomic state. An alternative approach has been to develop atom optics tools that are species independent such as transmission diffraction gratings and transmission Fresnel lenses [2, 3]. Atom optics with ground-state noble gases such as helium and neon has been limited to the latter approach due to the lack of accessible optical transitions. This fact makes control and detection problematic and thus work with these atoms has been much more limited. Nevertheless, ground-state noble gas atoms have two remarkable properties that make them ideal for atom optics and interferometry. First, very high intensity noble gas supersonic beams are readily available [4]. Second, atomically flat single-crystal surfaces such as Si and LiF reflect these atoms elastically with high probabilities [5]. In addition, single-crystal surfaces have well defined periodic structures and can also be used as diffraction gratings for atomic beams.

Atomic beams are traditionally created by allowing gas to escape from a

source with a small aperture and collimating the output. In the dilute-gas regime, where the mean free path is larger than the aperture size, the resulting beam has a very broad distribution in velocity as well as angle. As the pressure is increased in the source, the resulting beam becomes very monochromatic and directional, a property of supersonic expansion [4]. To reach the required pressures of several atmospheres, noble gases are typically used as the primary gas and they are "seeded" with another gas which is carried along. The best performance is obtained for a pure supersonic beam of helium where the highest pressure is possible.

The elastic scattering probability of a noble gas impinging on a single crystal surface is well described by the Debye-Waller factor and decreases exponentially with increasing incident energy [6]. Large improvements in elastic reflection probability can thus be obtained by lowering the velocity of the atoms.

In this thesis we describe an apparatus that combines these two features to slow a supersonic beam of ground-state helium by elastic reflection from a moving single crystal mounted on a spinning rotor. Doak et. al. suggested a similar experiment, however the estimated slow beam flux was only $6 \cdot 10^5$ atoms/s [7]. Simulations show that we should be able to increase the expected beam flux to 10^{11} atoms/s by using atom focusing and near normal reflection from the receding crystal. Moreover, we are using a supersonic nozzle that is able to achieve atom beam intensities as high as $4 \cdot 10^{23}$ atoms/s/sr.

To the best of our knowledge, Gupta and Herschbach demonstrated the only experimental realization of supersonic beam slowing by mounting the supersonic nozzle on a spinning rotor [8]. However, their continuously operating room temperature nozzle created a high background gas pressure that attenuated the slow beam by scattering and limited the final translational velocity of a 10^{12} atom/s Xenon beam to 70 m/s having a transverse temperature of several Kelvin.

We present first experimental results that show a slowing of a He:Ne mix-

ture from 510 m/s to velocities between 265 m/s and 510 m/s with a transverse temperature of 250 mK.

In chapter 2 we describe the principle of our apparatus. We follow the atoms from the supersonic valve through the slowing reflection from the rotor tip and several beam guiding reflections to the noble gas detector. We describe the apparatus as it was originally conceived and simulated although not all elements of it are yet experimentally realized.

In chapter 3 we present simulations which predict the key properties of our resulting beam. We simulate the effect of different rotational speeds and of a focusing element behind the slowing reflection on the resulting flux.

Chapter 4 describes in detail the vacuum chamber, the supersonic nozzle, the rotating system, the preparation and mounting of the mirror crystals, and the gas detector. Here, we also describe problems we experienced with the original design and how we have solved or plan to solve them.

In chapter 5 we present experimental results. We first analyze the original supersonic beam and verify its monochromaticity. Then we show that we can manipulate the velocity of the reflected beam by varying the rotor speed as predicted and calculate the resulting beam velocity as a function of the tip velocity. We show that we are able to slow a 510 m/s supersonic beam to 265 m/s.

Chapter 6 outlines future work and proposes possible uses for our slow beam. We also briefly present a new method of slowing atoms using pulsed high magnetic fields we are developing in parallel to the rotor experiment.

Chapter 2

The beam slowing apparatus

In this chapter we describe the essential components of our beam slowing apparatus. We follow the beam from its source, the supersonic nozzle, through the slowing reflection from the rotor tip and the collimating reflection from a focusing mirror to the beam detector.

2.1 High intensity cryogenic pulsed supersonic nozzle

The starting point of the beam path is the supersonic beam which is optimized with the development of a new high-pressure pulsed valve[9] developed by Prof. Uzi Even from the Tel Aviv University. The unique features of this valve are a pulse duration as short as $10\mu s$ FWHM at a repetition rate of up to 40 Hz, combined with cryogenic (77K) operation. The valve can operate with backing pressures of up to 100 atmospheres, leading to a supersonic beam in helium that is very directional (half-angle of 7°) and very monochromatic (less than 1% relative spread in velocity).

A 3D model of the valve is shown in figure 2.1(a) and a schematic drawing of the actual valve mechanism is presented in figure 2.1(b). The trumpet shaped nozzle is blocked by a plunger (green) which in turn is held by a spring (blue) from

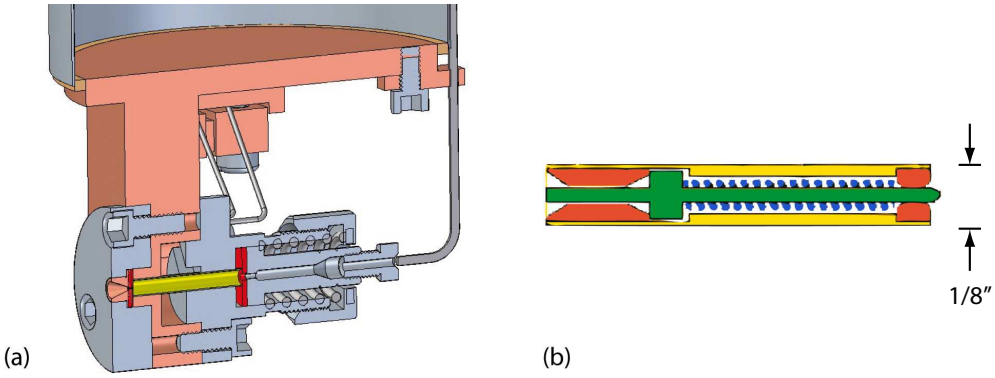

Figure 2.1: The cryogenic supersonic valve. (a) The conic nozzle is cooled by a liquid nitrogen cryostat. The valve mechanism is enclosed in a high pressure steel tube (yellow) which is sealed by two Kapton washers (red). The assembly is held together by a strong spring from the back. A coil (not shown) produces a short pulse of up to 2.5T to open the valve. (b) Detailed view of the high pressure steel tube. The valve is blocked by a plunger (green) which is guided by two ceramic washers (red) in a stainless steel tube (yellow). The magnetic field of the coil pulls the plunger about 150μm to the right. A small spring (blue) returns the plunger to its sealed position after the electromagnetic pulse.

the back. The coil of the nozzle can produce a magnetic field of 2.5 T for about 20 μs. The plunger is pulled back about 150 μm and is returned to its sealed position by the spring within 15 μs.

An estimate of the flux Φ from the nozzle is given by $\Phi \approx \frac{\rho \bar{v}}{4}$ where ρ is the number density and $\bar{v}$ is the mean velocity of the atoms. Operating the nozzle cryogenically at 77K and at a pressure of 30 atm, the mean velocity is about 900 m/s and so we calculate a flux of $\Phi \approx 6 \cdot 10^{29}$ atoms/m^2/s. Since the diameter of the nozzle is 200μm and the nozzle opening time is 10μs, we estimate the brightness of the beam to be $2 \cdot 10^{17}$ atoms/shot, which at the quoted repetition rate of 40 Hz translates to $8 \cdot 10^{18}$ atoms/s.

2.1.1 Gas flow in the supersonic regime

Atomic beams are produced by letting gas escape from a pressurized container into vacuum. In the effusive regime, where the mean free path of the gas particles is much larger than the dimensions of the aperture, a thermal beam with the well known Maxwellian velocity distribution

$$f(v) = \frac{4}{\sqrt{\pi}} \left(\frac{m}{2kT} \right)^{3/2} v^2 \exp(-mv^2/2kT) \tag{2.1}$$

is created. Here, m is the mass of a single gas particle, k is the Boltzmann constant and T the temperature.

The mean free path is proportional to temperature and inversely proportional to pressure. By raising the pressure in the gas container one reaches a regime where collisions during the gas dynamic expansion have to be taken into account. In this regime, the gas flow is governed by three equations. They are (in one dimension) the continuity equation which prohibits the spontaneous creation or annihilation of mass in the flow field

$$\frac{dw}{w} + \frac{d\rho}{\rho} + \frac{dA}{A} = 0, \tag{2.2}$$

the momentum equation

$$wdw + \frac{dP}{\rho} = 0, \tag{2.3}$$

and the energy equation

$$wdw + dh = 0. \tag{2.4}$$

Here w is the velocity of flow, ρ is the gas density, A is the cross sectional area of the tube in which the gas is flowing, P is the pressure and h the gas enthalpy

$$h = e + P/\rho \tag{2.5}$$

with the internal energy e. In the following deductions we will also use the ideal gas equation

$$P = \frac{R}{M}\rho T \tag{2.6}$$

where R is the universal gas constant and M the molar mass of the gas.

All thermodynamic quantities of the one dimensional flow of an ideal gas can be expressed using the specific heat ratio

$$\kappa = \frac{c_P}{c_V} \tag{2.7}$$

and the Mach number. The specific heats at constant pressure c_P and constant volume c_V are given by

$$c_p = \left(\frac{de}{dT}\right)_V \qquad \text{and} \qquad c_p = \left(\frac{dh}{dT}\right)_P \tag{2.8}$$

respectively. Differentiating 2.5 with respect to temperature using 2.6 and 2.8 yields:

$$c_P = c_V + \frac{R}{M} \tag{2.9}$$

and the often useful relations

$$c_V = \frac{1}{\kappa - 1}\frac{R}{M} \qquad \text{and} \qquad c_P = \frac{\kappa}{\kappa - 1}\frac{R}{M}. \tag{2.10}$$

The specific heat ratio of an ideal monatomic gas is $\kappa = 5/3$.

The Mach number

$$M = \frac{w}{c}. \tag{2.11}$$

is the ratio between the flow velocity ω and the speed of sound in the gas which can be shown to be [10]

$$c = \sqrt{\kappa\frac{P}{\rho}} = \sqrt{\kappa\frac{RT}{M}} \tag{2.12}$$

in an ideal gas. Since the speed of sound is proportional to the mean molecular speed in a gas, the Mach number is a measure for the ratio of directed motion to the random thermal molecular motion. A supersonic beam with a high Mach number is therefore very monochromatic.

For an isentropic flow (dq=0) one can show that [11]

$$\kappa \frac{d\rho}{\rho} = \frac{dP}{P} \tag{2.13}$$

and using 2.12

$$\frac{dP}{\rho} = c^2 \frac{d\rho}{\rho}. \tag{2.14}$$

The continuity equation now yields

$$\frac{dA}{A} + \frac{dw}{w}(1 - M^2) = 0. \tag{2.15}$$

We see that for subsonic flow ($M < 1$), the flow velocity increases with decreasing tube diameter. For supersonic flow ($M > 1$) however, the flow velocity *decreases* with decreasing tube diameter. To accelerate a gas to supersonic velocities one therefore has to build a nozzle that first converges and accelerates the gas to sonic speed and then diverges to further accelerate it to large Mach numbers. Such nozzles are called Laval nozzles, after the nineteenth century's Swedish engineer De Laval who first designed them to increase the speed of steam entering turbines.

Integrating the energy equation shows that the flow velocities at two different positions, labeled by the indices 0 and 1, are related by

$$\frac{w_1^2 - w_0^2}{2} = h_0 - h_1 = \int_{T_1}^{T_0} c_P dT = c_P T_0 (1 - \frac{T_1}{T_0}). \tag{2.16}$$

For a nozzle, we can choose point 0 in the gas reservoir, where $w_0 \approx 0$. The flow

velocity at any point in the nozzle is then (using 2.10):

$$w = \sqrt{2\frac{\kappa}{\kappa - 1}\frac{RT_0}{M}(1 - \frac{T}{T_0})} \tag{2.17}$$

Solving the relation for T yields

$$T = \frac{T_0}{1 + \frac{\kappa-1}{2}M^2}. \tag{2.18}$$

Thus, the higher the Mach number the, colder the beam.

So far, we described the expanding gas as a continuous medium in which thermal equilibrium is guaranteed at any point. This holds true if the flow properties change over a distance scale larger than the mean free path. In a supersonic beam, however, the density decreases rapidly as the gas expands into the vacuum and a transition to free molecular flow occurs during the expansion.

The theoretic treatment of this transition is rather difficult. However, it is still possible to calculate the beam temperature by replacing the Mach number with the speed ratio

$$S = \frac{w}{v_w} = \sqrt{\frac{\kappa}{2}}M \tag{2.19}$$

which is the ratio between the flow speed and the *most probable* relative speed in the gas. The temperature of a beam of ideal gas is then

$$T = \frac{T_0}{1 + \frac{\kappa-1}{\kappa}S^2} = \frac{T_0}{1 + \frac{2}{5}S^2}. \tag{2.20}$$

Experimentally, the speed ratio for a short pulse can be found by calculating the ratio between the arrival time and width of the beam signal. If one fits the measured pulse with a Gaussian curve with center t and width 2σ, the speed ratio is given by

$$S = \frac{t}{\sigma} = 2\sqrt{2ln(2)}\frac{t}{\Delta t_{FWHM}} \tag{2.21}$$

where Δt_{FWHM} is the full width at half maximum in time.

2.2 The rotor as a beam slower

Similar to the beam paddle that was developed for neutrons [12], we reduce the mean velocity of the supersonic beam by specularly reflecting the atoms from a single crystal Si(111) surface which moves along the beam direction. For a linearly moving mirror, the speed of the atoms after hitting the mirror is

$$v_f = -v_a + 2v_m, \tag{2.22}$$

where v_a is the initial velocity of the atoms, v_m is the velocity of the mirror, and v_f is the final velocity of the atoms. In order to slow the supersonic jet of $v_a = 900$ m/s helium atoms to a final velocity of $v_f = 50$ m/s, the speed of the reflecting surface has to be $\frac{1}{2}(v_a - v_f) = 425$ m/s.

It is technically hard, although not impossible, to construct a machine that can repeatedly move a surface with such high speeds. Our group has, with the help of UT's Center for Electromechanics, investigated the possibility of launching and catching a projectile with a coil gun system. But although we are convinced that such an apparatus could in principle be built, we decided to use a more feasible experimental setup.

High mirror velocities are readily achievable by mounting the reflecting surface on the tip of a spinning rotor. Rotary motion, however, creates an unwanted

fanning effect. Due to a finite nozzle opening time, the temporal extent of our atomic beam arriving at the spinning mirror is about 15 μs. Over this period of time the angle of reflecting mirror changes proportionally to the angular velocity ω, and the reflected atomic beam is spread in the rotation plane. To reduce the fanning effect without changing the mirror speed we can increase the rotor diameter and decrease the angular velocity. To achieve a tip velocity of 425 m/s a 1m long rotor has to spin with an angular velocity of $\omega = 843.8\ s^{-1}$ or 134.3 Hz.

2.3 Atomic mirrors and lenses

A perfect atom mirror has to be atomically flat over a length scale larger than the atomic beam diameter. Usually, atomically flat surfaces are prepared *in situ* by cleaving single crystals under ultra high vacuum. We cannot use this method to produce atomic mirrors, since the mirrors have to be mounted on the tips of our rotor. Fortunately, hydrogen passivated Si (111) surface, Si(111)-1×1H, can be easily prepared *ex-situ* by wet etching of a Si(111) wafer [13]. That allows us to mount the atom mirrors on the rotor tips at atmospheric pressure. Moreover, Allison et. al have shown that the helium reflectivity of a hydrogen passivated surface does not change over a period of several days in ultra high vacuum [14].

However, the passivated crystals can oxidize rapidly and it is therefore important to expose them as little as possible to air. A detailed description of the cleaning and etching process is given in section 4.3.2.

It is important to estimate the fraction of atoms that will be elastically scattered from the atomic mirror. For single crystal surfaces with zero well depth (no Beeby correction), the fraction of atoms elastically scattered is given by the Debye-Waller factor [15, 6],

$$\frac{I}{I_0} = e^{-2W} \tag{2.23}$$

$$2W = 24mE_{\perp}T_s/(Mk_B\theta_s^2) \tag{2.24}$$

where m is the mass of the impinging atom, M is the mass of the atom in the crystal, T_s is the temperature of the crystal, $E_{\perp}$ is the normal incident energy, and θ_s is the crystal Debye temperature [15].

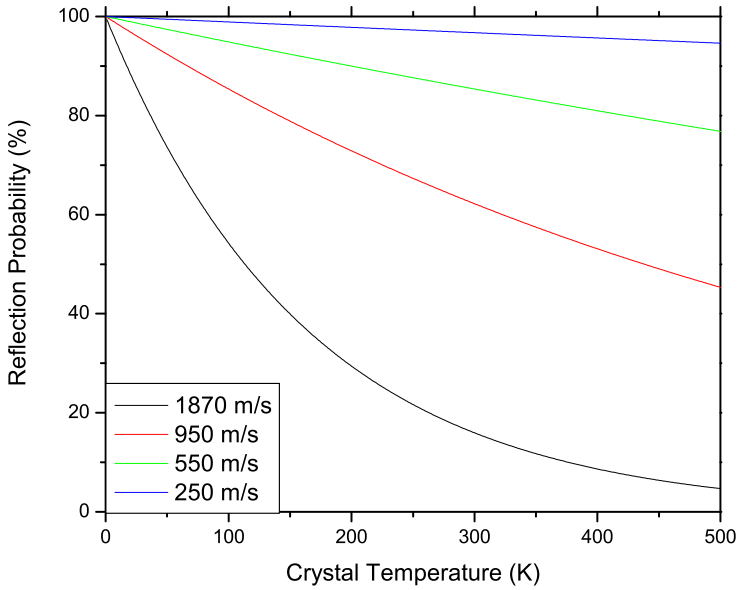

Figure 2.2: Debye Waller factor for helium reflecting from a Si (111) surface as a function of crystal temperature for various helium beam velocities.

The Debye Waller factor for helium reflecting from Si (111) as a function of crystal temperature is plotted in figure 2.2. For helium atoms coming from a room temperature supersonic nozzle ($v_a = 1870$ m/s) reflected from Si (111) surface kept at room temperature at 45° incidence the estimated reflectivity is 37.7%. The specular reflectivity is lowered by impurities, steps or etch pits on the surface and by

the distribution of the beam intensity over about 40 open diffraction channels (the crystal momentum of 111 Si is 1.89 $Å^{-1}$ which corresponds to a Helium velocity of 299.8 m/s). Thus it is not surprising that the experimental specular reflectivity is below 10% at these conditions [16]. We expect to see higher reflectivity from the moving crystal since the relative velocity of helium atoms reflecting from it is more than three times smaller. The Debye-Waller factor at this speed (425 m/s) is 0.9 and only the 6 first order diffraction channels remain open.

At slow beam velocities below 300m/s reflection probabilities are well above 90% and no diffraction channels are allowed. However, at these low velocities quantum effects become important and the exact value of the reflectivity is still an open question.

The inherent divergence of the supersonic beam leads to the loss of useful flux. The rotor fanning effect contributes further to the loss of flux by spreading the beam in the rotation plane. However, the detrimental effects of beam divergence and fanning can be mitigated by focusing the atomic beam using reflection from a curved mirror surface. The focal length of the focusing mirror has to be close to the distance between the tip of the rotor and the mirror itself. This distance should be minimized to increase the number of atoms hitting the focus mirror after reflection from the rotor. In our design, the distance from rotor tip to focusing mirror is 16cm.

Doak et. al. have shown helium beam focusing using Fresnel zone plates, however due to microfabrication resolution limitations, the zone plate diameter was only 0.27 mm [3]. Allison et al. [17] have demonstrated helium beam focusing using a thin Si wafer bent electrostatically. The minimal focal length achieved using this method is too long for our purposes. Therefore, we are using a fixed focal length design where the silicon wafer is mechanically clamped between two round rings with angled faces. The angle depends on the width of the opening and the desired focal length. We can achieve a focal length as small as 17 cm before breaking a

225 μm thick wafer. To achieve high flux through a wide range of atom speeds, we choose the focal length to be 20 cm (see chapter 3).

2.4 Noble gas atom detector

Detection of the atoms is a crucial step since the high flux would be wasted if it could not be detected. We use a modified quadrupole mass analyzer for the detection of the atoms. The Residual Gas Analyzer (RGA) from SRS [18] we are using is equipped with an optional electron multiplier (CDEM). We can measure the current produced by the impinging ions with a data acquisition card that is installed in a personal computer and directly connected to the CDEM. We can therefore use the instrument as it is originally intended to analyze the background pressure in our chamber when the CDEM is switched off or we can measure the profile and intensity of the incoming noble gas beam by switching the CDEM on and bypassing the slow electronics of the RGA.

The detection efficiency of such a device for room temperature helium is on the order of 10^{-5} [19]. Since the ionization probability scales linearly with the transit time through the ionizer, we believe that our detection efficiency will be better by about an order of magnitude.

Chapter 3

Simulation of the beam

Parallel to designing the hardware, we did extensive simulations of the planned system to optimize the design parameters that influence the slow beam flux. In this chapter we describe the system we simulate, the method of simulation, and the most important conclusions we draw from the simulations.

3.1 Simulated system and simulation method

We use a Monte Carlo method to simulate the beam slowing and focusing process. Each run starts with 200 million atoms having Gaussian velocity distribution of 32 m/s FWHM centered around 900 m/s in the propagation direction. The velocity distribution in both transverse directions is 110 m/s FWHM centered at zero. Our simulations only included atoms within two standard deviations of the mean for both the transverse and longitudinal velocity distributions. This, however, should not influence the results of the simulation. Atoms with a transverse velocity that deviates more than two standard deviations from the beam will not fly through the various apertures. Atoms with a much too small or large longitudinal velocity will either miss the crystal on the rotor tip or will be reflected from it in a too large or

too small angle respectively so that they miss the focusing mirror.

Atoms that are blocked by an aperture or miss a reflecting surface are considered lost and are not counted toward the final flux. The final flux is normalized to the expected output flux of the supersonic nozzle, $\Phi = 1.2 \cdot 10^{18}$ atoms/s.

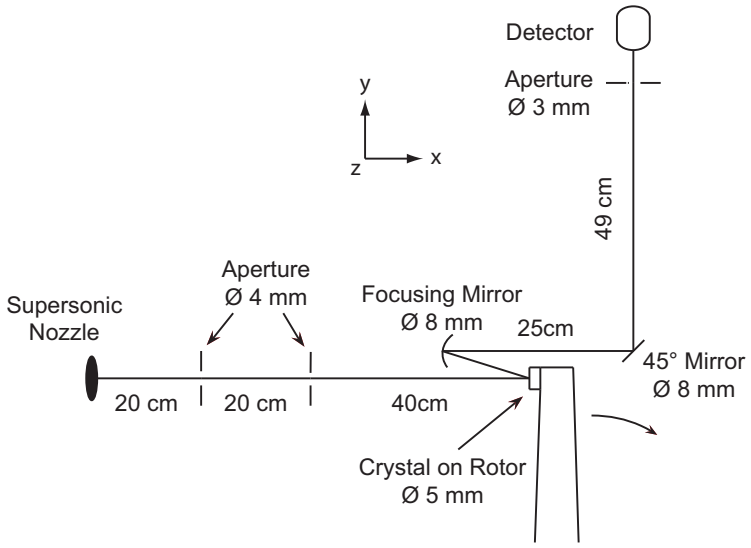

Figure 3.1: Schematic drawing of the proposed beam slower apparatus. The atomic beam is collimated by two apertures. It is then slowed by reflection from the moving rotor, focused by a curved mirror and finally deflected by a second mirror into the detector.

We now outline the beam path of the simulated system. First, the atomic beam is created at the location of the supersonic nozzle over a period of 10 μs. The beam is then collimated by two 4 mm apertures spaced 20 cm apart (see figure 3.1). The collimated beam is slowed by a collision with the receding 5 mm diameter crystal located 40 cm away from the last collimating aperture. The slowed beam is focused by an 8 mm diameter concave mirror and is directed to the final 3 mm aperture by a flat 8 mm diameter mirror rotated by 45°with respect to the propagation direction. The distance between the final aperture and the rotor-mounted mirror is 1 meter. The reflection probability of the atomic mirrors used in our simulations is given by

the Debye-Waller factor (equation 2.24).

For various final beam velocities, the rotor velocity as well as the position where the atoms hit the mirror changes. The mirror at the tip of the rotor is tilted clockwise by 1° in the horizontal plane so that if the rotor is moving with a tip velocity of 425m/s (final beam velocity 50m/s) atoms hit the tip exactly when the rotor is perpendicular to the beam. A stationary rotor (final beam velocity 900m/s) has to be placed 5° further back than the perpendicular position to guide the reflected atoms toward the focusing mirror. Consequently, the horizontal tilt of the focusing mirror also has to be adjusted to reflect the slow beam toward the second 45° mirror. At first glimpse, this might seem strange because we are used to thinking of a photon reflecting from a mirror where we can easily neglect the motion of the mirror. When reflecting a particle moving with comparable speed to the mirror itself, however, the angle of reflection is *not* the angle of incidence. This is also why the mirror is only tilted by 1° and not by 6° as it would have to be if it reflected light (the angle between the incoming beam and the reflected is 12°). In practice this means that we cannot align the mirrors with a laser prior to shooting atoms with the nozzle. In the simulations we kept the tilt of the mirror on the rotor tip constant and adjusted the phase of the rotor and the tilt of the focusing mirror accordingly.

3.2 Results of the simulation

3.2.1 Expected flux

We present the simulated beam flux as a function of slow beam velocity and mirror focal length in figure 3.2. Simulation results show that the flux through the final aperture decreases with final beam velocity. This can be explained in the following way: To achieve a slower beam velocity, the rotor has to move faster and the fanning

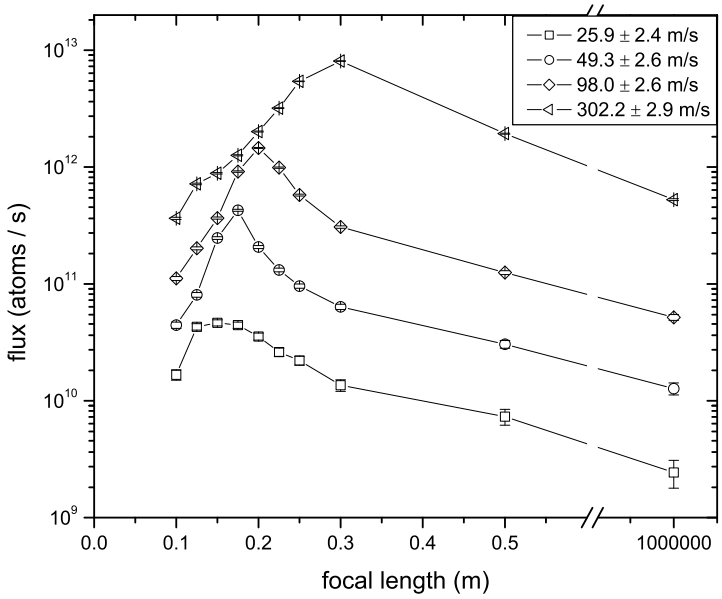

Figure 3.2: Atom flux after passing through the final aperture as a function of focal length for different slowed beam speeds. We observe flux gains of more than one order of magnitude from focusing.

effect increases the spread in the rotation plane. Consequently, more atoms miss the focusing mirror and the flux decreases. It should be noted though that even for the lowest simulated speed of 25 m/s the flux is well above 10^{10} atoms/s when using the optimal focal length of the atomic lens.

3.2.2 Influence of the focusing mirror

For all final beam velocities, the focusing of the beam increases the flux by more than one order of magnitude. The optimal focal length depends on the speed and increases from 15 cm at 25 m/s to 30 cm at 302 m/s. To illustrate the focusing effect we present the transverse position distributions of a 49 m/s beam at the plane of the final 3 mm aperture. Figure 3.3 (a) shows the position distribution for an infinite

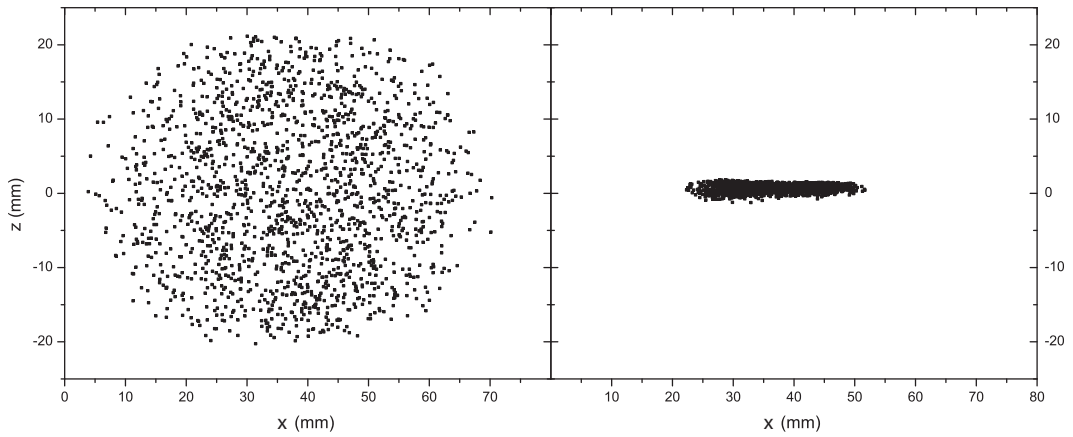

Figure 3.3: Spatial distribution of atoms at the location of the final aperture. Simulated slow beam velocity is 49 m/s in both cases. (a) infinitely long focal length (standard deviation of 10.35 cm in the z-direction and 13.5 cm in the x-direction) (b) focal length of 17.5 cm (standard deviation of 0.49 cm in the z-direction and 6.3 cm in the x-direction)

focal length mirror (flat mirror), whereas figure 3.3 (b) shows the distribution for the optimal focal length of 17.5 cm. Comparing the standard deviations of the distributions, it can be seen that the mirror indeed compensates the fanning effect (the spread of the atoms in plane of the rotor) by a factor of two. The increase in flux, however, results mainly from the focusing in the z-direction, which reduces the spread in z by a factor of 20. The reason we cannot focus as well in the plane of the rotor is that the fanning effect makes the rotor appear as a source of finite extent in the rotor plane.

3.2.3 Energy resolution of the beam

A closer examination of the velocity distribution of the slowed beam reveals a useful correlation between the speed and the arrival time of an atom at a specific point in space. In figure 3.4 the longitudinal velocity of each atom is plotted against the time that has passed from the opening of the nozzle to its arrival at the aperture.

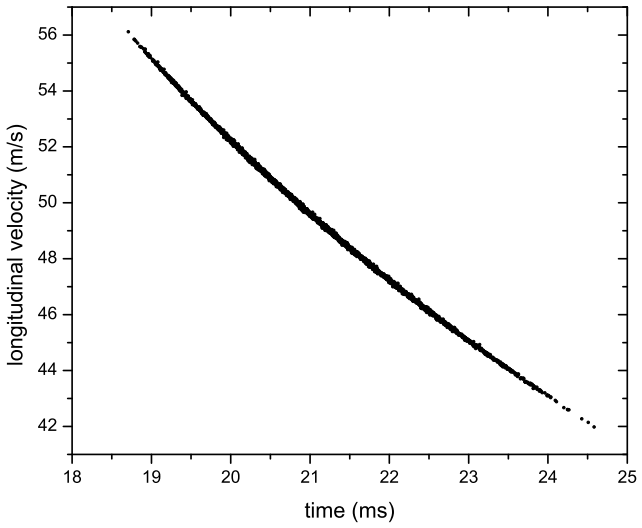

Figure 3.4: Correlation between the velocity and arrival time after passing through the final 3 mm aperture.

The fastest atoms arrive more than 5 ms earlier than the slowest and there is a very strong correlation between time and velocity. An analysis of this correlation shows that by measuring the arrival time with microsecond resolution, the velocity resolution is greater than 10 cm/s which corresponds to an energy resolution of about 1.5 μeV.

Chapter 4

Designing and building the vacuum chamber and rotor assembly

Having described the general properties of our apparatus in chapter 2 and presented the expected beam properties of such a device in chapter 3, we now go into more detail and describe the parts that were actually built and assembled. The design of almost all parts was done with the CAD program Solid Edge [20]. We are therefore able to present detailed 3D models next to actual photographs that should help the reader understand the function of each part.

Figure 4.1 shows an overview of the vacuum system that was simulated in chapter 3. The nozzle (green) is located in a 6-way cross, the two skimmers (green) are mounted in an attached 4-way cross. The rotor (yellow) spins inside the pancake shaped "rotor chamber" and which is attached to the rectangular "mirror chamber" containing the focusing mirror and the 45° mirror (red). The atoms are detected with an RGA (blue). The the second mirror was first left out intentionally to allow detection of the direct and the reflected beam with the RGA mounted on a flange

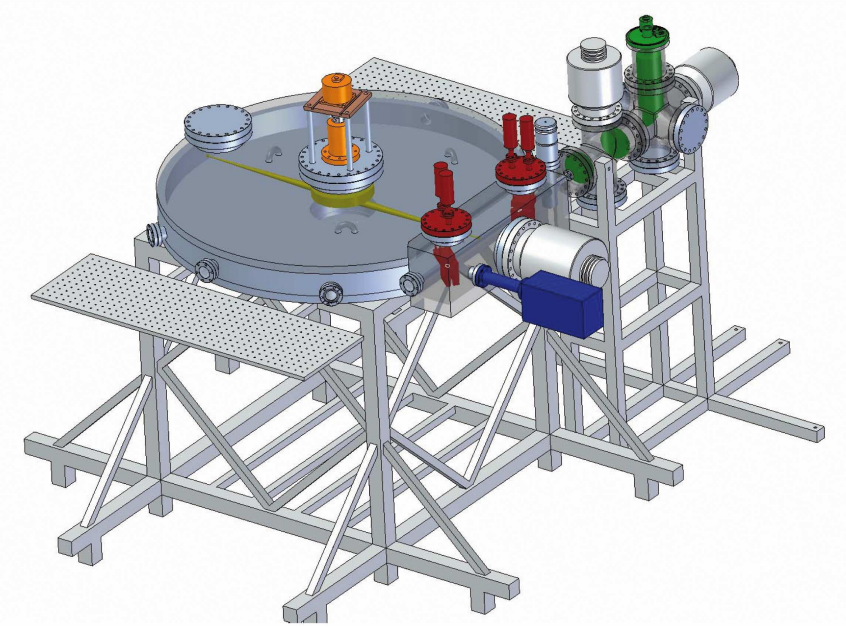

Figure 4.1: Model of the beam slowing apparatus as simulated in chapter 3. The beam is produced by the pulsed cryogenic supersonic nozzle (green) and passes through two skimmers (green). It is reflected from the tip of the spinning rotor (yellow) to the focusing mirror (red) which focuses it via a 45° mirror to the RGA (blue).

opposing the nozzle.

With the help of Prof. Even, who was visiting our lab during the first two months of the experiment, we soon realized that we had to change several aspects of the setup to optimize the profile of the supersonic beam. Also, we first had to decrease the number of degrees of freedom in the experiment and simplify the beam path to prove that beam slowing is possible in principle. An overview of the chamber as it stands now in our lab is shown in figure 4.2. The most obvious changes are the additional RGA opposing the nozzle which is used to characterize the direct beam, and the replacement of the focusing mirror with a second RGA which detects the slow beam directly after the reflection from the rotor.

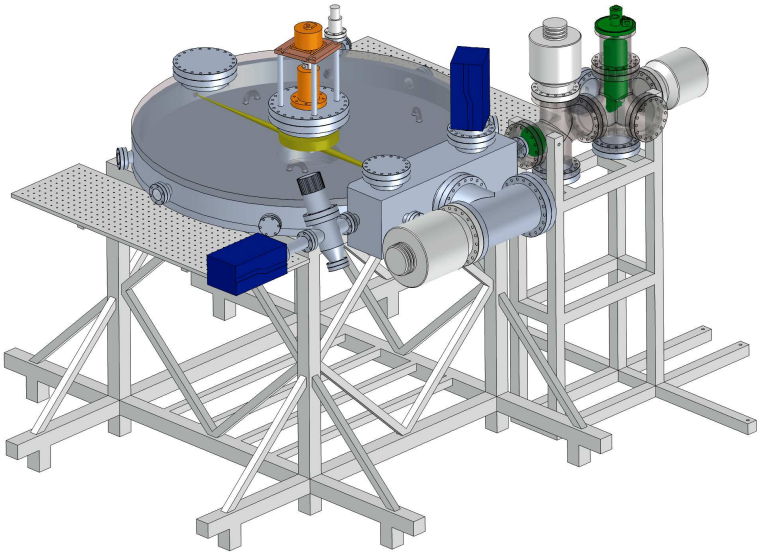

Figure 4.2: Model of the beam slowing apparatus as it is assembled in our laboratory. The two mirrors have been removed to simplify the experiment and a second RGA has been mounted instead of the focusing mirror. The RGA 100 (opposing the nozzle) is used to characterize the direct beam, the other (RGA 200) detects the reflected and slowed beam.

4.1 The vacuum chamber

Because of the large rotor diameter, the vacuum chamber itself has to be fairly large. Due to the high surface area of the rotor housing, the atmospheric pressure is exerting a force equivalent to that of several tons on the chamber. It is therefore built from one inch thick stainless steel plates. Still, we can measure the top and bottom plate of the chamber being pulled together by 4 mm when we pump out the chamber. This obviously also lowers the tip of the rotor but this can be taken into account when aligning the nozzle.

The chamber weighs approximately half a ton and is supported by a hollow rod aluminum structure. About 300 kg of weights are placed on the bottom grid

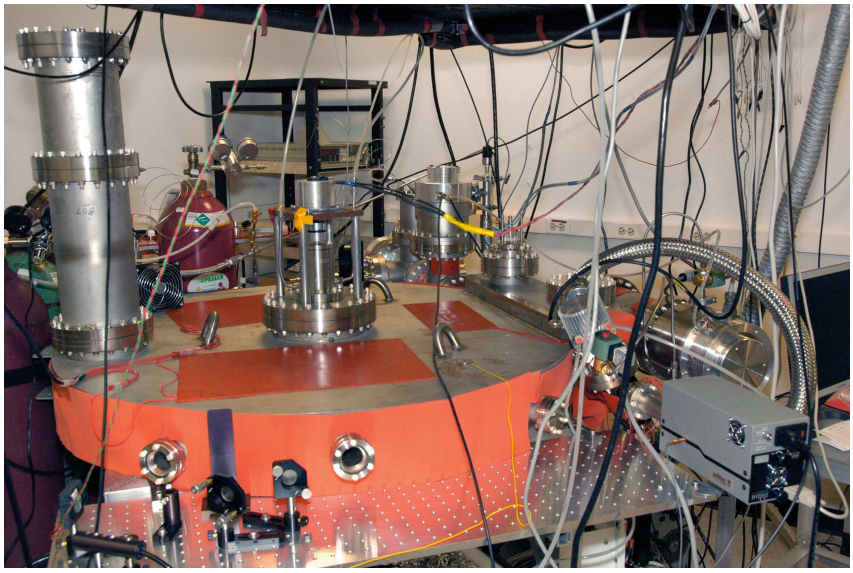

Figure 4.3: Photo of our beam slowing apparatus. The orange pads on the rotor chamber are surface heating pads for bakeout, the orange foam is heat isolation. The tall metal tube on the left houses a cold finger.

of the support structure to lower the center of mass. Four legs of the structure are filled with silicon rubber for vibration absorption. For the same reason, silicon rubber filled tubes are sandwiched between the chamber and the support structure.

The rotary feedthrough (orange in figure 4.2) and the spindle (yellow) are lowered into the chamber through the central 10 inch flange. The rotor itself (yellow) is put in through the 8 inch flange on the mirror chamber. The main turbo pump (500 l/s pump speed) is mounted on this flange via an 8 inch tee after the rotor is put into the chamber. The rotor is then fastened to the spindle through the 10 inch flange on the bottom of the chamber. The 8 inch flange opposing the mirror chamber provides access to the rotor tips to mount the crystals.

The six view ports at the side of the rotor chamber provide optical access for the dynamical balancing which is described in section 4.2.1 and for a laser that is periodically cut by the rotor and can serve as a trigger for the nozzle. Note that

the motor controller produces a TTL pulse at a predefined rotor position which we use to trigger the valve. A cold cathode ion gauge is mounted on one of the ports to measure the pressure in the rotor chamber.

The nozzle chamber is connected to the mirror chamber by a flexible bellows to allow alignment of the nozzle and skimmers with the tip of the rotor. After aligning, the 1.33 inch bellows we first used was bent in such a way that it was nearly completely blocking the beam. Also, the gate valve we had first installed was mounted on a 1.33 inch flange so that the beam had to pass through a 6 inch long narrow tubing which lead to beam broadening. We therefore removed the gate valve and replaced the 1.33 inch bellows with a 2.75 inch bellows.

The nozzle itself (green) is lowered into the first cross through the top 6 inch flange. A cold cathode ion gauge (not visible) is mounted on one side flange to measure the pressure in this first chamber.

The conical skimmers (green) are made of 60 μm thin nickel foil and are very fragile. They are held by lock rings that are screwed into disks which in turn are inserted into the second cross. The disks are firmly held in place by O-rings and fixed at three spots each with Torr Seal, a vacuum compatible adhesive. The skimmer closer to the nozzle is momentarily removed because we believed it to cause disturbances in the beam which create a high pressure "tail" after the beam pulse. Since we achieve pressures in the 10^{-8} torr range we are not concerned about the resulting loss of the differential pumping of the chamber. However, we have found out by now that the main reason for this tail was the lack of a differentially pumped "detector chamber" (see section 4.4.1) and we will probably reinsert the skimmer in the future. The two crosses are pumped with two 300l turbo pumps (light grey).

The whole system can be aligned by looking with a telescope from the end of the mirror chamber through the tip of the rotor, the gate valve, and the skimmers toward the nozzle. Screws on the nozzle support structure are used to adjust height,

left-right position and tilt in each direction.

Heating pads glued to the top and bottom of the chamber, around the two crosses, around the tee for the main pump and around the tee that houses the detector with a total power of 4.8 kW, are used to bake out the chamber. Whenever we break vacuum, the chamber is filled with dry nitrogen. If we have to open it, a nitrogen overpressure is maintained to minimize air inflow and afterward the chamber is heated to 120°C overnight. Base pressures of 5×10^{-9} torr can thus be readily obtained. We found that we can still pump the chamber down to a pressure of 8×10^{-9} torr after opening the 8 inch flange for a few minutes to exchange the crystals on the rotor tip. We therefore do not bake the chamber after exchanging the crystals.

4.2 The rotor and spindle

Figure 4.4 shows the parts described in the following section.

The rotor is spun by a 380 Watt stepper motor which we can operate with a simple LabView[21] program via a Galil MC controller[23]. The motor is equipped with a 8000 line encoder for closed loop operation which provides an angle resolution of 0.045°. It is elastically coupled to the shaft of a ferrofluidic vacuum rotary feedthrough from Ferrotec[22]. A ferrofluid is a stable colloidal suspension of sub-domain magnetic particles in a liquid carrier. In a gradient field, the whole fluid responds as a homogeneous magnetic liquid which moves to the region of highest flux. This means that ferrofluids can be precisely positioned and controlled by an external magnetic field. In a vacuum rotary feedthrough, the fluid forms an O-ring between a protrusion from the pole piece that sourrounds a permanent magnet and the magnetically permeable shaft (see figure 4.5) that can hold a pressure difference up to 200mbar. Our feedthrough utilizes 10 of these stages with a low vapor pressure ferrofluid and is able to hold a vacuum up to 10^{-10} torr.

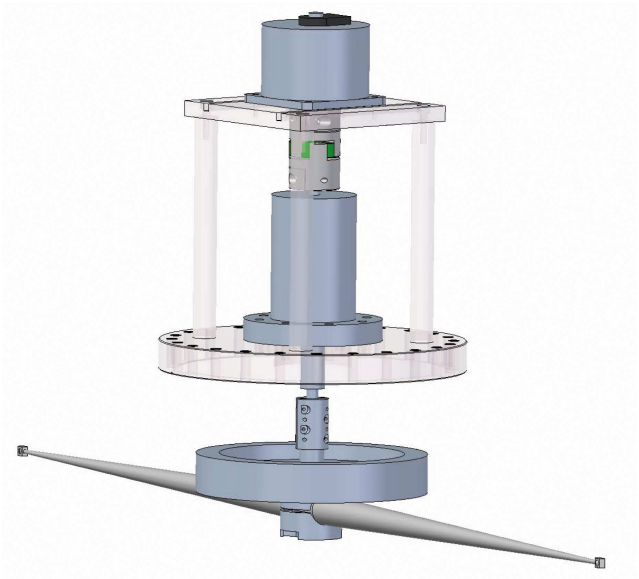

Figure 4.4: Detailed view of the spinning parts. The motor is flexible coupled to a ferrofluidic feedthrough. Inside the vacuum chamber, the feedthrough shaft is rigidly coupled to the spindle which holds the rotor. The large disk of the spindle increases the moment of inertia around the spinning axis and can hold screws for balancing.

Inside the vacuum chamber, the shaft of the feedthrough is rigidly coupled to a spindle which in turn holds the rotor itself. The rotor is not supported from the bottom so that its motion is not constrained. Nonetheless, it may be possible to dampen out vibration by some dissipative mechanism under the rotor. We were considering a spring-loaded sapphire puck on which the rotor would spin and which would dissipate vibration energy by friction. We also considered an inductive vibration reduction that consisted of a magnet mounted on the rotor and a copper plate mounted closely below it. As long as there was no vibration, the magnet would rotate with the rotor around its symmetry axis and the magnetic flux through any part of the copper would be constant in time. If the rotor started to vibrate in a pendulum mode, the flux through the copper would vary and a current would be induced in the copper which in turn would dampen out the pendulum motion. On

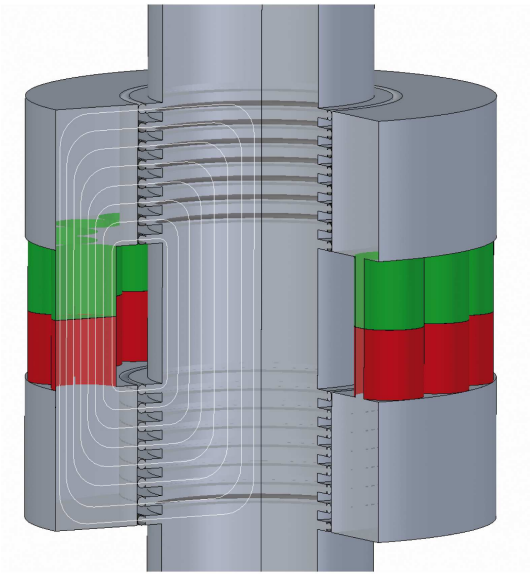

Figure 4.5: Working principle of the ferrofluidic feedthrough. The spinning shaft is surrounded by several strong magnets. The field lines are guided by two pole pieces and concentrated where metal rings are protruding from the shaft. The ferrofluid is pulled into the regions with highest magnetic flux and forms O-rings between the pole piece and the protrusions.

closer inspection, both solutions proved to have a much too little effect and provide no dampening of a shaft twisting mode or a "butterfly" mode where the rotor tips move up and down. We are currently operating without any damping mechanism.

An object rotates stably only around its axis of lowest or highest moment of inertia. The axis of lowest moment is clearly along the rotor but since the rotor is nearly rotationally symmetric it was originally not clear whether it would spin around the axis with the highest moment. As advised by the engineers from the Center for Electromechanics, we added a disk to the spindle to insure this. Its mass is concentrated on the outer diameter to provide maximum moment of inertia while keeping the overall mass as low as possible. The total mass of the spinning parts (coupling, spindle and rotor) is 5.1 kg, the total moment of inertia is 0.013 kgm^2 along the rotor axis, 0.053 kgm^2 along the axis of rotation and 0.043 kgm^2 along

the axis perpendicular to the latter. When the rotor is spinning with 130 Hz, its kinetic energy is 17.7 kJ.

Along the rim of the spindle 14 tapped holes provide a means of dynamically balancing the rotating mass. By putting small set screws at the correct positions, we can compensate for inherent imbalance produced by inevitable machining inaccuracies.

Figure 4.6: Model of the rotor and closeup of the tip. The rotor length is 101.5 cm and it tapers down from 1 inch in the center to 1/8 inch at the tip. The crystal is inserted in the hole on the tip from the back and held against a lip in the front by an aluminum setscrew.

The rotor itself (see figure 4.6) is a 101.5 cm long tapered rod with a cubic mirror holder on each end machined out of grade 5 titanium alloy. The silicon crystal is held in the tip by a lock ring that presses it against a lip at the front end of the threaded hole.

The shape of the rotor is optimized for maximum tensile strength using a finite element analysis program[24]. Figure 4.7 shows the calculated tensile stress acting on the rotor when spinning at 140 Hz. The maximum stress is 152MPa which is only 5 times less than the yield tensile strength of the titanium alloy. This is the

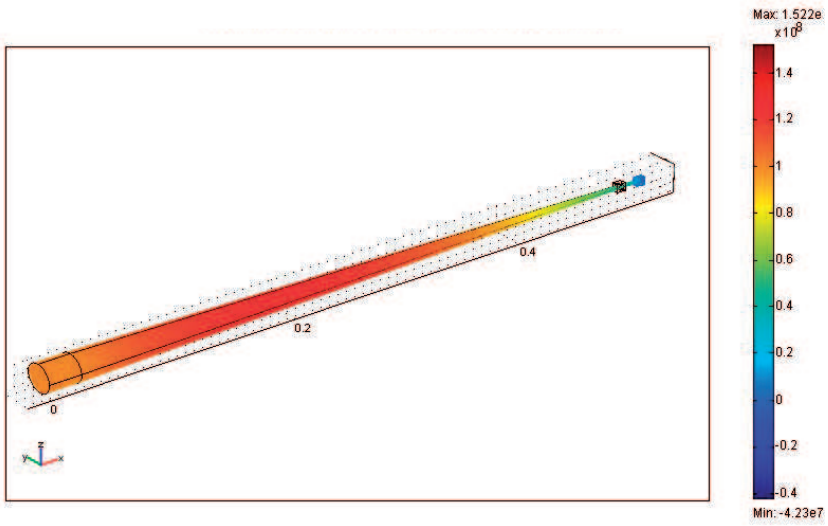

Figure 4.7: Tensile stress acting on the rotor when spinning with 140 Hz. The stress is largest at a distance of about 20cm from the axis of rotation were it is only 5 times smaller than the yield tensile strength of the titanium alloy.

reason why the crystals on the rotor tip are limited to a diameter of only 5mm.

When we balanced the rotor it soon became apparent that with the current design we would not be able to spin faster then 42 Hz (see next section). The tensile stress scales quadratically with the rotation velocity so that the maximum stress at 40 Hz is 60 times lower than the yield tensile strength. We therefore built two mirror holders for crystals with a diameter of 1/2 inch (see figure 4.8) which are screwed into the rotor tip. Besides the 6 times larger area, they also have the advantage that the crystals are now much easier to mount on the rotor tip. The crystals are clamped between a circular plate and a lock ring when they are taken out of the etching solution. This easy to handle assembly is then screwed into a third piece which in turn is permanently screwed into the original thread on the rotor tip. Once we are able to spin at higher frequencies (which probably requires redesigning the

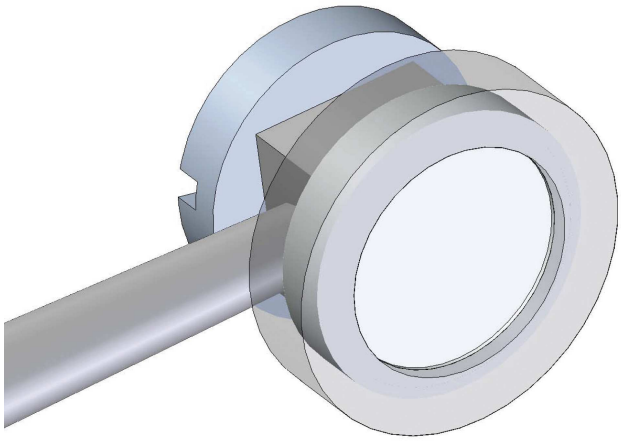

Figure 4.8: Detail view of the rotor tip with a mounted holder for the larger (0.5inch) Si wafer. A stainless steel screw (light blue) is inserted from the back into the hole in the rotor tip. The wafer is clamped between a plate and a lock ring (transparent) outside the vacuum chamber. This assembly can then easily be screwed on the previously mounted screw.

spindle, see next section) we can easily remove the larger holder and return to the small crystals.

4.2.1 Balancing the rotor

All rotating parts are machined with a precision of $\pm\frac{1}{1000}$ inch and are statically balanced. However, even the most carefully machined part will not be perfect and the smallest static imbalance might cause large vibrations when rotating the system.

We measure vibration in two different ways. With our first detection method utilizing a laser we are able to measure the absolute amplitude of shaft pendulum modes with a resolution of 5 μm. We pass a laser beam from one view port through the rotor chamber to the opposing view port at which we detect the transmitted intensity with a photo diode. We now align the beam so that half of it is blocked by the lower spindle part holding the rotor. If the shaft vibrates, the spindle will periodically move left and right and block more and less of the beam which results

in a periodic modulation of the photo current.

To calibrate the photo diode, we first redirect the laser beam with a mirror toward a knife edge mounted on a translation stage and measure the transmitted intensity as a function of the position of the knife edge when we sweep it through the beam. Since the beam has a Gaussian profile we can fit the measured intensities with an error function. We could now produce a table relating the measured photo current with the position of the knife edge or spindle respectively. But since we are only operating in the central, linear part of the error function, we can simply multiply the measured amplitude of the variation of the photo current with the slope of the error function in its center and know the amplitude of the vibration of the shaft. We correct the multiplication factor by taking into account the measured intensity loss after passing through two view ports.

In the second method, we rigidly mount an accelerometer on the outer wall of the rotor chamber to detect vibrations of the whole system. This way we are sure to detect any mode of vibration (twisting and pendulum modes of the shaft and butterfly modes of the rotor) but we can not measure its absolute amplitude. Resonances, however, are easily detectable and by comparing the signal of the accelerometer with the signal from our laser vibration measurement method we can set an upper limit when we believe the vibrations to become too large.

We find that the shaft has a runout which we were only able to minimize to 70 μm by assembling the spinning parts while monitoring it with a feeler gauge.

We measure the vibration with both methods at different speeds and with different trial weights screwed into different holes in the spindle. An typical measurement of the vibration amplitudes for different rotation speeds is shown in figure 4.9.

We are not able to determine any combination of balancing weights that decreases the vibrations significantly and therefore run the rotor without any balancing

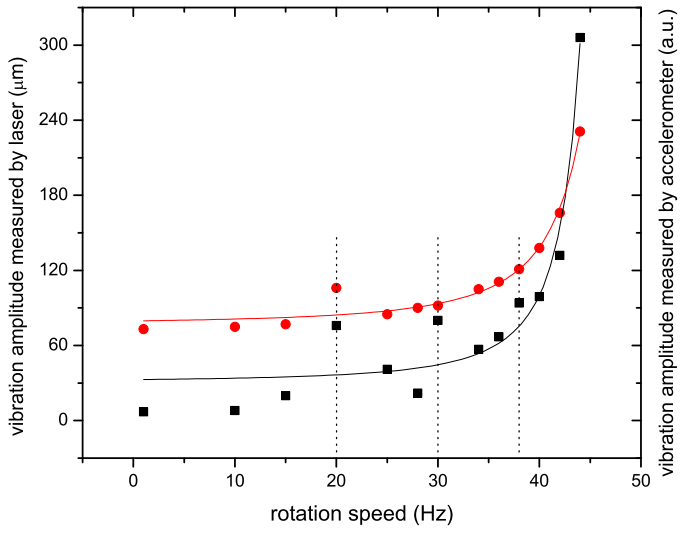

Figure 4.9: Vibration amplitude at different rotation speeds measured with laser (red) and accelerometer (black). The dotted lines indicate the location of three prominent resonances at 20, 30 and 38 Hz, the solid lines are Lorentzian curves fitted to the measured data to predict the location and magnitude of the limiting resonance.

weights in place. The resonances occurring at 20, 30 and 38 Hz and especially the large resonance at around 50 Hz are not affected by balancing. However, we believe that dynamic balancing will become more effective and important at higher speeds and smaller initial runout.

A look at the power spectrum of the measured signal reveals that some rotation speeds excite resonances at higher harmonics of the rotation frequency. At 20 Hz rotation speed, for example, the system vibrates with 40 Hz and the measured photo current is a pure 40 Hz sine wave. Accelerating as fast as possible to "run" through a resonance does not seem safer than slowly sweeping through it. If we slowly increase the rotation speed when we approach a resonance and measure the vibration amplitude, we can fit the measured data with a Lorentzian and estimate

the amplitude of the vibration at the resonance frequency. The increase of vibration when approaching 45 Hz is only the shoulder of a resonance peak centered between 48 and 50 Hz with a vibration amplitude of 1000 to 2000 μm, depending what data set we fit. We are not able to pass this resonance safely and are therefore limited to a maximum rotation speed of less than 42 Hz.

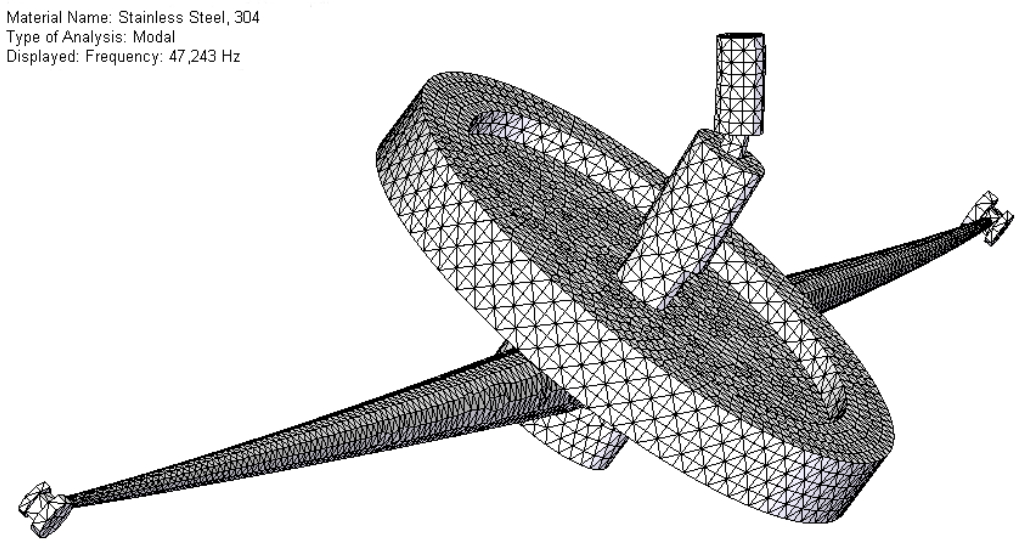

Figure 4.10: The limiting pendulum eigenmode at 47Hz of the spinning system calculated via finite element analysis.

A finite element analysis[20] of the rotating parts shows qualitatively the nature of the resonances. We calculate that the shaft has two pendulum modes with eigenfrequencies of 34Hz and 47Hz (see figure 4.10) and a twisting mode at 35Hz . The mismatch between the calculated and measured frequencies has several reasons. In the finite element analysis used, we can not assign a different material

to the rotor than to the spindle. We treat the whole spinning assembly as one part made out of stainless steel which would weigh about 700 g more than the actual part. The real resonance frequencies should therefore be higher than the calculated. The main source for inaccuracy of the simulation is that we do not know how the shaft is held in the ferrofluidic feedthrough and can therefore not model the constraints correctly. Nevertheless, the finite element analysis convinces us that the resonance frequencies of the spinning system lie between 30 and 50 Hz which agrees with our measurement.

The only ways to shift these resonances to higher frequencies is to either increase the shaft diameter or lower the moment of inertia of the spindle and the rotor. We cannot increase the thickness of the shaft coming from the ferrofluidic feedthrough, but we can clamp it over its complete length and thus make an effectively stiffer shaft. We will also have to decrease the mass of the spinning parts. The easiest way to do both of these is to exchange the spindle. The finite element analysis shows that by simply cutting off the thick outer rim of the spindle, the limiting pendulum frequency is shifted to 65Hz. By doing this, however, the system would no longer spin around the axis with the highest moment of inertia. We cannot predict if this would have a noticeable effect. Using a longer coupling that encloses the thin part of the feedthrough shaft completely shifts the pendulum mode further up to 106 Hz.

A new spindle design will also use a different mechanism, similar to a collet used in commercial tool holders, to couple to the feedthrough shaft and a V-groove to clamp the rotor in place. Both are self centering and will decrease the potential for inherent runout.

4.3 Atomic mirrors and mirror holders

4.3.1 Atomic mirrors

We use hydrogen passivated silicon Si(111)-H(1×1) wafers with a low miss cut of ±0.1° as atomic mirrors. Since we needed 5mm small crystals for the rotor tip and 1 inch wafers for the two succeeding mirrors we decided to buy much larger wafers and cut out several smaller wafers from each. This is very cost effective; the price difference between a 1 inch wafer and a 4 inch wafer with the same specifications, for example, is negligible since the cutting and polishing of the wafer require the same amount of work.

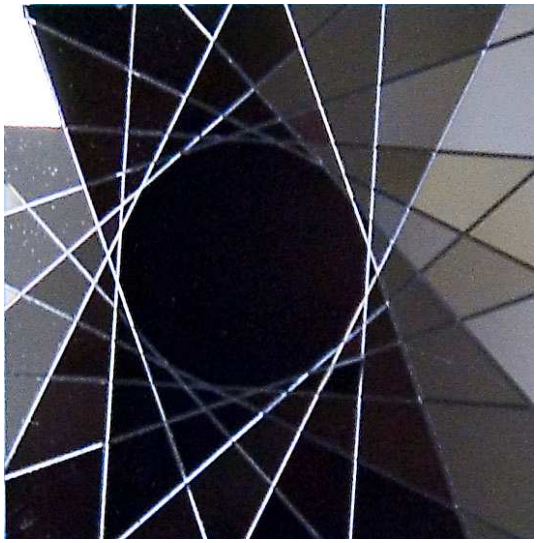

Figure 4.11: Hexagonal pattern cut from a larger Si wafer with a programmable dicing saw. Wafers of varying diameter can be produced on campus this way.

We first bought 13 phosphor doped 200 μm ± 20 μm thick and 10 cm wide wafers and sent them to Directed Light[25], a company that is specialized in precision laser cutting. We received back about 80 1 inch wafers and about 200 wafers that fit into the rotor tip. It turns out, however, that in the used cutting method the laser is guided by a water jet. Fine silicon dust in the water spray scratches the

silicon wafer which becomes effectively unusable up to a distance of 2 mm from the cut. This does not pose a problem for the larger crystals since they are clamped at the edge anyway and only the central part is intended as a reflecting surface. The small crystals, however, are unusable for our purpose and we also changed the size of the wafers for the rotor tip to 1/2 inch.

We solve this problem by cutting a 16 sided polygon from the center of a 1 inch wafer by combining four programs of an programmable dicing saw to cut 4 squares, rotated by 22.5° against each other (see figure 4.11). For our purpose, this hexadecagon is a good enough approximation of a circle and we can cut wafers in any size we desire.

4.3.2 Cleaning and etching procedure of the atom mirrors

To produce an atomically flat, passivated Si surface, one first has to clean the surface of organic residues and then etch the thin layer of silicon oxide. We use a procedure based on suggestions made by Alexander Khajetoorians, a fellow grad student from Dr. Ken Shih's lab here at UT and experiences of Dr. Bill Allison's Surface Physics Group in Cambridge.

All chemicals are LP grade or better, the ammonium fluoride for the critical last step is MB grade. The water used is ultra pure with a resistivity greater than 17 MΩcm. All bottles or beakers containing the chemicals and water and the tools used to handle the wafers are made of PTFE or PFA (Teflon). The cleaning and etching is done under the lab fume hood which is padded with clean room wipes.

To clean the wafer from dust and grease we first sonicate it for 10 min in isopropanol and for another 5 min in acetone. An RCA I solution (named after Radio Corporation of America Labs, where it was developed in 1965) is then used to remove organic residues from the surface and grow a uniform oxide layer. The solution consists of 1 part 30% ammonium hydroxide and one part 30% hydrogen

peroxide in 5 parts water. The water is heated to 80°C in a water bath before the ammonium hydroxide and the hydrogen peroxide are added and the wafer is submerged in the solution. A magnetic steerer provides mixing.

It is important to clean the wafer thoroughly under running water (at least three quarters of a liter) before etching it in the next step. RCA I is a strong oxidant and even small traces of it in the etching solution would result in an increased number of etch pits.

The optimal etching time depends on the thickness of the oxide layer and we found 15 min to be ideal for our wafers. Shorter times leave some oxide on the surface; longer times result in over-etched wafers. The etching solution is 40% ammonium fluoride which was first purged with ultra pure argon for at least 40 min to deplete it of dissolved oxygen. It should *not* be stirred or purged during the etching itself to avoid recontamination of the wafer with particles floating on the surface of the solution and even removing small hydrogen bubbles forming on the rim of the wafer with Teflon tweezers was found to do more harm than good. After the etching, a thorough rinse under running water is important to avoid over etching.

Figure 4.12 shows atomic force microscope images of the surface of an etched Si crystal. The left image (a) shows a clean surface with only little oxidation. One can clearly see the atomically flat terraces that stretch over several hundred nm. The image on the right (b) shows the same crystal 28 minutes later. The surface has become rougher and specs of silicon oxide become visible. A look at the profile along the indicated lines (figure 4.12 (c) and (d)) shows that the surface corrugation has already drastically increased. The longer one waits, the more of these specs appear until the surface becomes very grainy and finally smoother again because it is nearly completely oxidized.

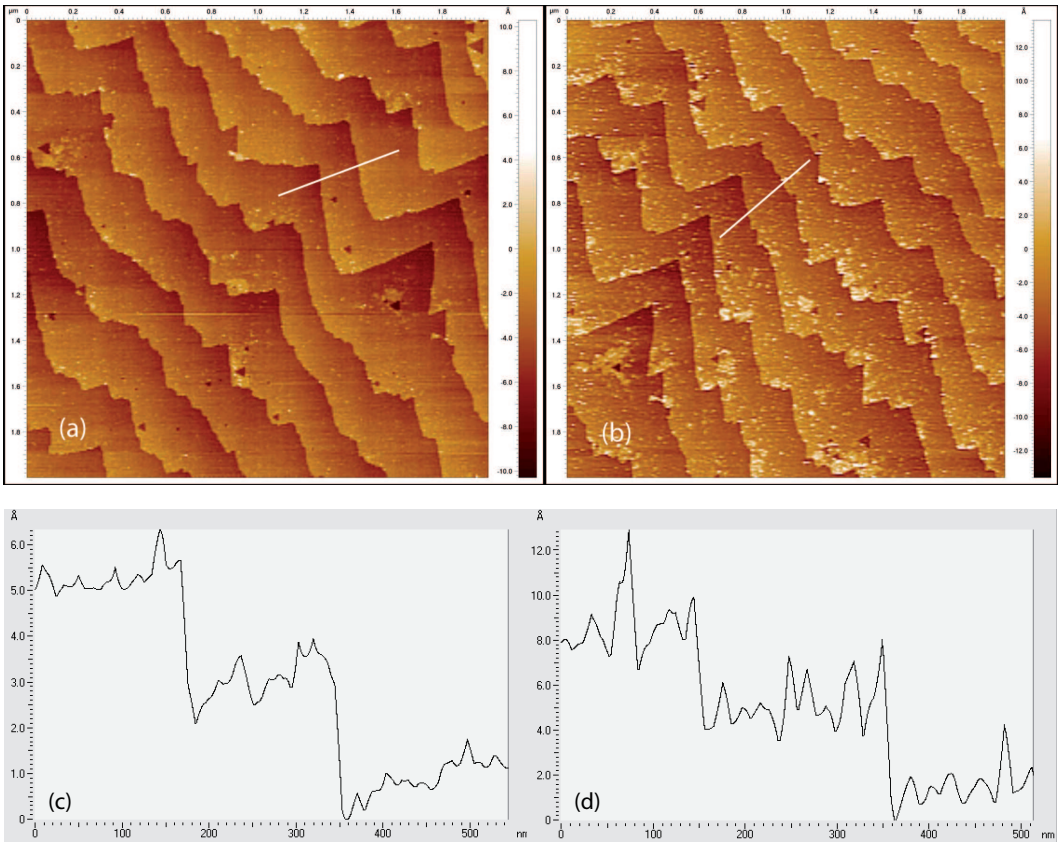

Figure 4.12: AFM images (2 μm $\times$ 2 μm) of a passivated Si wafer (a) 15 minutes and (b) 43 minutes after taking it out of the etching solution. The lines running from the upper left to the lower right are single atom steps, 2.5 Å high. The number of oxidized areas (light grains) increases drastically from the left to the right image. This can also be seen in the height profiles (c) and (d) taken along the white lines in (a) and (b) respectively. The surface corrugation directly after etching (c) is smaller than 1Å, the corrugation of the oxidized surface (d) on the other hand is on the order of 1 Å to 2 Å.

It is therefore critical to minimize the time the passivated surface is exposed to oxygen. We found that oxidation can already be observed after just a few minutes.

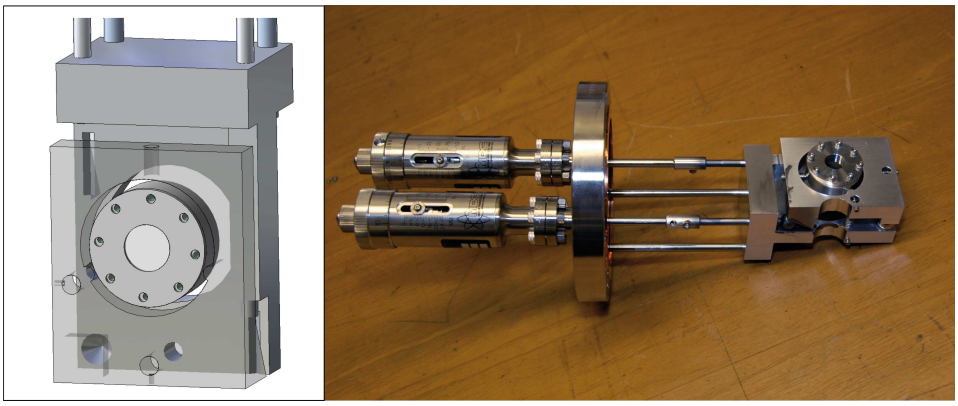

Figure 4.13: Model and photo of the mirror mount for the focusing mirror. The central piece clamps and bends the silicon wafer. The front piece (transparent) holds the clamp and can be tilted with two rods pressing on the angled surfaces via two steel balls. The insertion length of the rods and therefore the tilt angle can be adjusted with two micrometers from above. The right micrometer adjusts left-right tilt, the left micrometer adjusts up-down tilt.

4.3.3 Mirror holder and clamp

The focussing mirror as well as the second 45°deflecting mirror need to be adjustable in tilt and yaw *in situ* during alignment and later on when different atom speeds are desired. They are therefore mounted on adjustable mirror mounts, the design is shown in figure 4.13. The back part of the mirror mount is suspended from a 6 inch flange by two stainless steel rods. The height of the mirror can be changed by sliding the back part up and down on these rods. Tilt and yaw are controlled *in situ* via two linear vacuum feedthroughs from the top which push on two stainless steel balls. These transfer the vertical motion to a horizontal motion of the spring-loaded front part by sliding on its two triangular protrusions. The upper ball thus controls vertical tilt while the lower ball controls horizontal yaw. The stainless steel balls and the surfaces on which they slide are coated with Molybdenum Disulfide, a high vacuum compatible lubricant.

The part that actually clamps and, in the case of the focusing mirror, bends

the wafer is held in place by a single setscrew and can be easily removed. It consists of an aluminum ring whose upper face is concave and a matching cover ring with a convex surface. A silicon wafer clamped between the two faces will bend so that it forms a concave mirror (see figure 4.14).

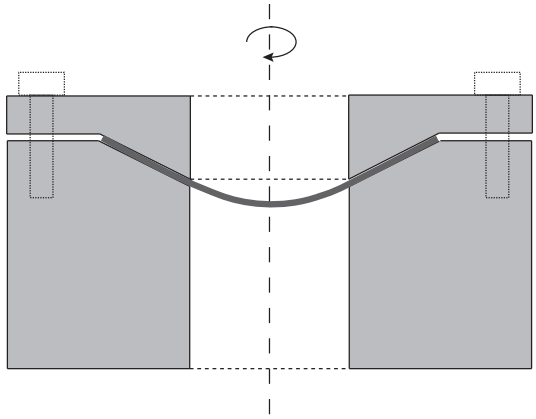

Figure 4.14: Schematic drawing of the mirror clamp. The silicon wafer (dark grey) is clamped between two rings with angled faces which causes it to bend. The angle in the drawing is highly exaggerated.

The angle of the clamping surface is determined by the desired focal length and the inner radius of the ring. Imagine a parabolic concave mirror with focal length f. The equation of a radial cross section of this mirror is

$$z(r) = \frac{1}{4f} r^2. \tag{4.1}$$

The angle α of the slope at each distance from the center is given by the derivative with respect to r:

$$\alpha(r) = \arctan[z'(r)] = \arctan[\frac{1}{2f} r] \tag{4.2}$$

In reverse, that means that if we want to clamp our silicon wafer in between two rings with inner diameter r so that it forms a concave mirror with focal length f, the face of the clamp has to be angled by the angle α given by the above equation.

The outer diameter of the mirror clamp is 1.5 inch, the inner diameter is 5/8 inch, and the desired focal length is 20cm. The clamping faces should therefore be angled by 1.1°.

We had to gradually increase the tilt of the cutting tool up to 1.6° until we ended up with the desired focal length. It is not clear if the real slope of the clamp is 1.1° as calculated and the reading on the lathe is inaccurate or if the angle is indeed larger because the mirror doesn't bend parabolically as assumed in the short derivation above.

4.4 Atom detector

Although we have built the focusing mirror and mounted it in the beam path, we found that adjusting the rotor phase and the two angles of the mirror allows too many degrees of freedom. Since the two reflections lower the flux significantly, we were not able to find a reflected beam with the focusing mirror in place. We replaced it, therefore, with a second detector with which we could successfully detect the reflected and slowed beam.

It is impossible to detect noble gases in the ground state, however, metastable atoms or ions can easily be detected with a multichannel plate or a simple Faraday cup. In our setup we use two modified SRS RGA residual gas analyzers[18]. The three crucial parts of every RGA are an ionizer, followed by a mass filter and an ion detector.

Figure 4.15 shows a schematic view of the RGA. The ionizer consists of a heated and negatively biased thoria coated iridium filament that produces free electrons around a grounded cathode cylinder. The filament is surrounded by a repeller grid that is negatively biased with respect to the filament. It reflects the produced electrons so that they pass multiple times through the ionization region before reaching the cathode. It also protects the fragile filament when inserting the

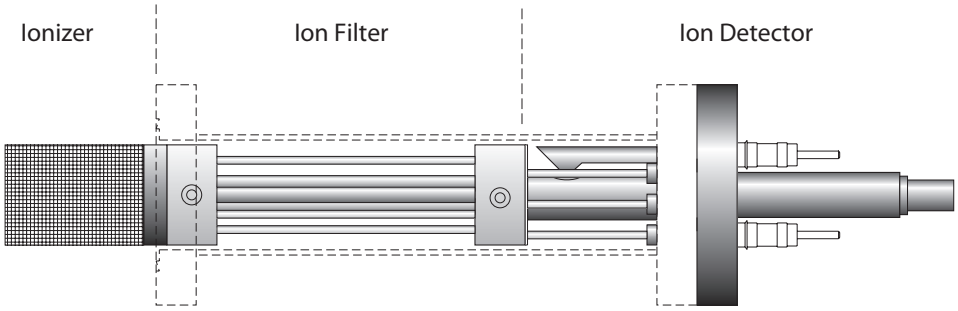

Figure 4.15: Schematic drawing of the RGA. Incoming atoms are ionized and focused into the quadrupole mass filter. The ions are detected with a Faraday cup or an electron multiplier. [26]

RGA into the flange. The kinetic energy of the electrons can be adjusted by the bias voltage of the filament and can ionize an incoming atom upon impact. The detection probability is about 10^{-5} for room temperature atoms and scales linearly with the time the atom spends in the ionization region. Helium atoms slowed to 50m/s should therefore have a 36 times higher ionization probability than room temperature helium atoms which move with a speed of about 1800m/s.

The ionizer is followed by a positively biased focusing ring that guides the ions toward the quadrupole mass filter. The mass filter consists of four cylindrical rods which are driven with a radio frequency alternating voltage (see figure 4.16). One rod pair is connected to a positive DC voltage upon which a sinusoidal RF voltage (2.7648MHz) is superimposed. The other rod pair is connected to a negative DC voltage upon which a sinusoidal RF voltage is superimposed, 180° out of phase with the RF voltage of the first set of rods.

Light ions (low mass-to-charge ratio) are able to follow the alternating component of the field. For the X direction, those ions will stay in phase with the RF drive, gain energy from the field and oscillate with increasingly large amplitudes until they encounter one of the rods and are discharged. Therefore, the X direction is a high-pass mass filter. On the other hand, in the Y direction, heavy ions will

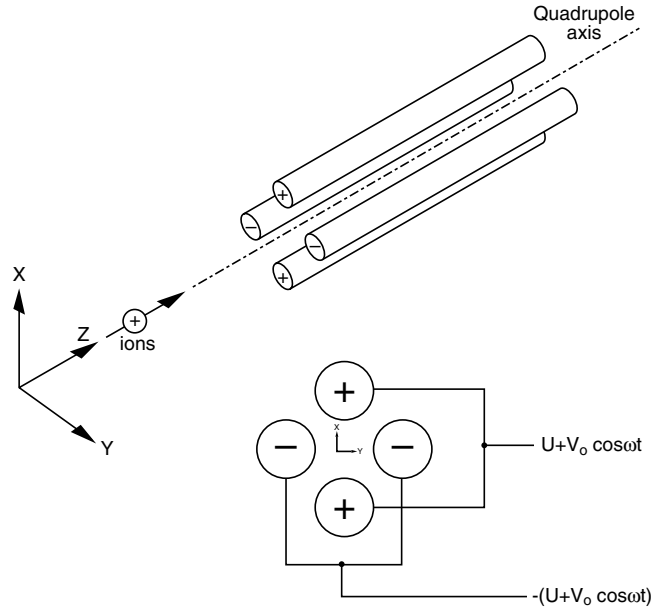

Figure 4.16: Working principle of the quadrupole mass filter. [26]

be unstable because of the defocusing effect of the DC component, but some lighter ions will be stabilized by the alternating component if its magnitude and amplitude are such as to correct the trajectory whenever its amplitude tends to increase. Thus, the Y direction is a low-pass mass filter. The quadrupole, if driven with the correct DC and RF voltages allows only ions with a certain mass-to-charge ratio to fly through. It is factory calibrated and operated by the internal electronics of the RGA, the user can only specify the desired mass-to-charge ratio. The alignment of the focusing plate with the rods is very important and a misaligned system can lead to reduced resolution or signal broadening in time.

The ion detector is a simple Faraday cup which produces a current with the same magnitude as the ion current. When a positively charged ion hits the grounded metal cup it gets neutralized by an electron in the metal. The produced currents are very small: 10^{-9} A for a pressure of 10^{-5} torr. Nevertheless minimum partial

pressures as low as 10^{-11} are in principle measurable with the Faraday cup.

For increased sensitivity an off axis mounted Macro Multi-Channel Continuous Dynode Electron Multiplier (CDEM) can be biased with a negative high voltage so that the ions are drawn away from the Faraday cup and hit the CDEM instead. It consists of 4 to 6 tubes of special resistive glass with a cone of the same material attached to its front. If an ion hits the surface of the cone it produces several secondary electrons. These are accelerated down the channels and create secondary electrons of their own and so on. Due to this avalanche effect, depending on the bias voltage, gain factors of 10 to 10^7 can be achieved.

Since we determine the final beam speed by a time of flight measurement, we cannot rely on the slow RGA electronics unit. Both our RGAs are therefore outfitted with a direct output of the current produced by the CDEM that is in turn amplified by an SRS low noise, high bandwidth preamplifier. This signal is directly recorded by a National Instruments data acquisition card.

We are using an RGA 100 with a mass range of 1 to 100 amu and an RGA 200 with a range from 1 to 200 amu. The main difference between the two models is the maximal supply voltage available to the rods.

4.4.1 Beam broadening in the RGAs

When we first studied the original beam, coming from the nozzle and detected by an RGA 100 at the opposing flange, we expected a Gaussian pulse shape with a half max half width of 20 to 30 μs. The measured beam profile however showed a shoulder starting at about 50 μs after the expected main beam, about half the amplitude of the beam and exponentially decaying withing a few hundred microseconds.

In 50 μs, a 1800 m/s fast atom travels 9 cm, so the shoulder was probably the result of a reflection or scattering of the beam from a surface that is maximally 5 cm away from the beam itself. This lead us to the conclusion that the beam interacted

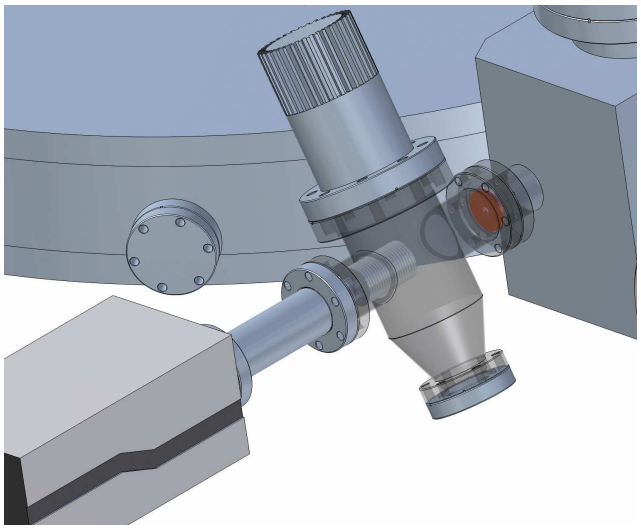

Figure 4.17: Model of the RGA 100 mounted opposite the nozzle for characterization of the direct beam. The beam is dumped into the RGA and quickly pumped away by a 70l turbo pump mounted closely to the ionization region of the RGA.

with an obstacle in its path or with the walls of a narrow tube it is passing through.

We removed the 1.33 inch narrow gate valve and replaced the 1.33 inch bellows connecting the nozzle chamber and the mirror chamber with a 2.75 inch bellows. We also removed the first skimmer which might have been too close to the nozzle and which therefore might have introduced turbulences in the gas flow. Unfortunately none of these measures reduced the intensity or width of the shoulder.

Finally we realized that we were dumping the complete beam into the RGA and that only a small portion of the beam is ionized and detected when it is flying through the ionizer. The majority of atoms are not ionized and thermalize with the walls of the RGA. Most of these atoms eventually bounce back into the ionization region and are detected.

To prevent this, we mounted a 70l turbo pump on a tee close to the ionizer of the RGA and inserted an aperture at the front end of the tee (see figure 4.17). Now, the RGA has its own, differentially pumped "detection chamber" and atoms

that are not ionized on the first pass of the ionization region get quickly pumped away. This reduced the shoulder behind the beam to about 1/16 of the signal.

The RGA 200, which is detecting the reflected beam, is lowered into the chamber through the 6 inch flange which will later house the focusing mirror. Thus, there is no aperture in front of this RGA and it is not be differentially pumped. The original beam has widened to a more than 2 inch diameter when it hits the back wall of the mirror chamber. A part of the beam, therefore, thermalizes with the wall of the mirror chamber and eventually reaches the ionization region of the RGA 200. We indeed see a very broad (up to 1 ms wide) background resulting from this when the nozzle is turned on. The amplitude of the maximum is about one percent of the original beam amplitude.

Chapter 5

Experimental results

For a better understanding of the following chapter and to remind the reader of the most important components of the slowing apparatus, previously described in detail, a schematic 2D cross section of the chamber with the beam path is shown in figure 5.1.

5.1 The direct supersonic beam

We first use the RGA 100 to characterize the direct beam when the rotor is turned out of the way. The pulse arrives $t = 800\mu s$ after the nozzle receives the TTL signal to open and has a width of $\Delta t = 20\mu s$ FWHM. This width is comparable to the nozzle opening time of 10 μs, so that equation 2.21 can only give a lower limit for the speed ratio. The driver electronics of the nozzle cause a delay of its opening of $t_d = 40\mu s$. The speed ratio is therefore at least $S = 2\sqrt{2ln(2)}\frac{t-t_d}{\Delta t} = 89$ and the temperature of the beam according to equation 2.20 is less than 94 mK. The velocity of the beam is $1.42m/760\mu s = 1868m/s$. By measuring the total charge produced by the CDEM and taking into account gain and ionization probability we estimate the intensity of the beam to be 2×10^{11} atoms per pulse.

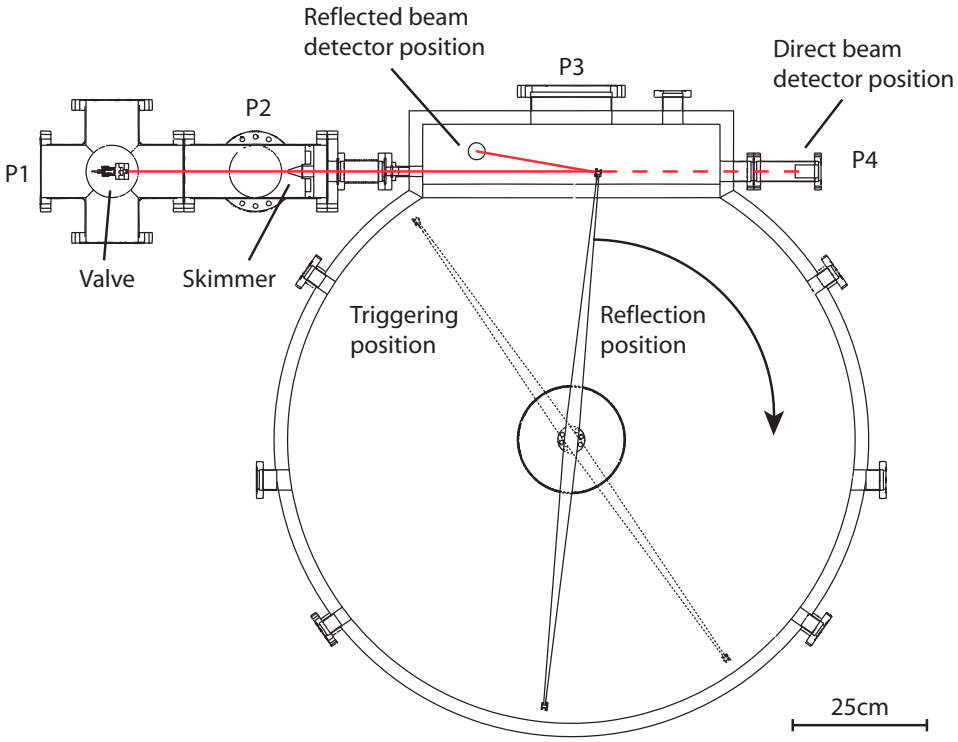

Figure 5.1: Schematic of the chamber with beam path (red). The valve is triggered when the rotor is 30 °away from the reflecting position . P1 through P4 are the pump locations.

Because we are currently limited to rotation frequencies smaller than 42 Hz (tip speeds of less than 132m/s) we decided to first slow the original beam to lower speeds with conventional methods before braking it further with our rotor.

There are two ways of slowing the beam before the reflection from the rotor. First, one can cool the nozzle, preferably to cryogenic temperatures. Using the energy relation

$$\frac{3}{2}kT = \frac{1}{2}mv^2 \tag{5.1}$$

one can easily see that the beam velocity v scales with the square root of the source temperature T. Cooling the nozzle to liquid nitrogen temperature we expect a beam with a velocity of $v_{cryo} = \sqrt{\frac{77K}{300K}}1868m/s = 946m/s$.

To further slow the original beam, one can seed the Helium with a carrier gas. A mixture of 50% He and 50% Ne behaves in first approximation like a single gas with mass $m = \frac{4+20}{2} = 12$. Assuming that the pure gas and the mixture have the same kinetic energy at a given temperature

$$\frac{1}{2}mv^2 = \frac{1}{2}m'v'^2 \tag{5.2}$$

one finds that the velocity scales with the square root of the mass ratio. A He:Ne mixture at cryogenic temperature should therefore yield a beam velocity of $v_{mix} = \sqrt{\frac{4}{12}} \times 946m/s = 546m/s$.

Figure 5.2 shows the measured flux vs. time profile of such a beam (black). The pulse arrives at 2776 μs $\pm$ 30μs with a width of 200 μs $\pm$ 15 μs FWHM. The speed ratio is 28 $\pm$ 2, the temperature 249 mK $\pm$ 36 mK. The atoms have traveled 142 cm $\pm$ 1 cm from the nozzle to the detector. The beam velocity is therefore 519 m/s $\pm$ 9 m/s.

The red curve in figure 5.2 is the signal of the beam reflected from the stationary rotor tip. It is detected with the RGA 200 and the travelling distance is only 111 cm, which results in the shorter arrival time. Most importantly, the beam temperature is 254 mK $\pm$ 41 mK. This confirms that the beam is not heated by the reflection.

It might seem to the reader now that an arbitrary low beam velocity can be achieved by simply cooling to lower and lower temperatures and seeding with much heavier gases. Why, one could ask, do we need the rotor at all?

Cooling with liquid nitrogen is simple and inexpensive. To achieve even lower temperatures one has to cool with more expensive Helium and the experiment becomes extremely hard to control.

A second problem is the formation of clusters. Although He_n has the lowest binding energy of any gas molecule it is not surprising that near liquid helium

temperature even helium gas begins to condensate into clusters. Heavier gases cluster already at liquid nitrogen temperature. Clustering results in a broad shoulder corresponding to a high beam temperature which makes the beam useless for many applications like precision surface analysis.

Because the nozzle is operated with a backing pressure of only 2 atmospheres (as opposed to 50 atmospheres for the pure He beam) the beam intensity is lowered by about three orders of magnitude. Higher pressures would again result in the formation of Ne clusters.

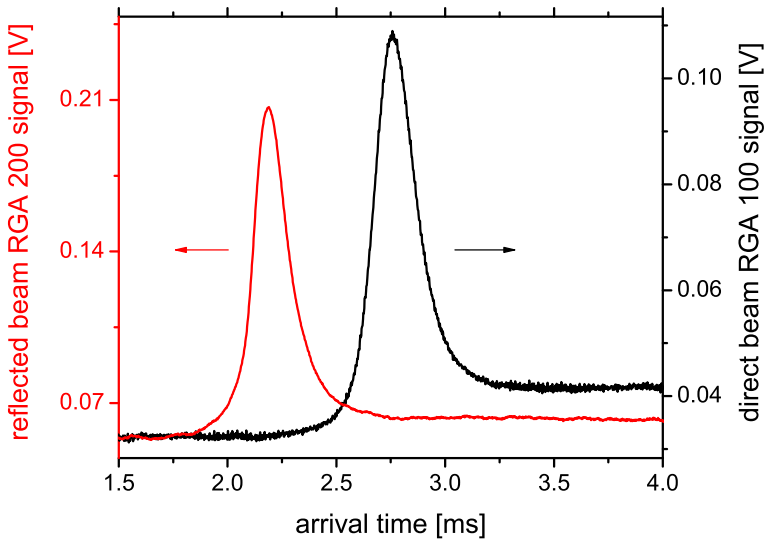

Figure 5.2: The direct cryogenic 48:52 He:Ne beam signal (black) and the signal of the beam reflected from the stationary rotor (red). Shown is the average over 50 measurements. The different arrival times result from different travelling lengths to the detectors. The signals have different heights due to different detector geometries and CDEM gains and do not allow us to draw any conclusions about reflectivity. The temperature of the direct beam is 249 mK $\pm$ 36 mK, the temperature of the reflected beam is 254 mK $\pm$ 41 mK; the reflection does not heat the beam.

The He:Ne mixture at liquid nitrogen temperature produces the slow, cluster free beam we need for the proof of principle experiment.

5.2 The slowed beam

The opening of the nozzle has to be timed exactly so that the puff of gas emitted hits the rotor when it is in the right position to reflect the gas into the detector.

The correct position changes with the rotational speed since angle of incidence and reflection are not the same at higher speeds (see also section 3.1). In fact, when the rotor stands still, due to the angled tip, its offset from the perpendicular position is about 5.5°, as shown in figure 5.1. The higher the rotation speed, the closer the rotor is to being perpendicular to the beam when it intercepts it.

The motor controller produces a TTL pulse when the rotor is 24.5° away from the perpendicular position (see figue 5.1). After a predefined delay, the computer sends a second TTL pulse to start the nozzle and starts recording the ion current from the detector. We first calculate the delay for a given speed and then optimize it to yield the brightest reflection. We then increase and decrease the delay to a maximum and minimum value until the height of the reflected beam signal is half its maximum height. The delay we use to record data is then the arithmetic average of the so found maximum and minimum and is mostly identical to the delay that gave the maximum beam intensity. The error in delay we take as half of the difference between the two extrema.

Figure 5.3 shows the recorded peaks at different rotation speeds. Clearly, the beam has been significantly slowed by the reflection at higher speeds. The decrease in intensity with higher speeds can be explained by the increasing fanning effect.

For each speed we fit Gaussian curves to 50 measured reflections. The mean of the centers of the fitted curves is taken as the arrival time, the standard deviation as the error. The arrival time of the reflected beam changes a little from shot to

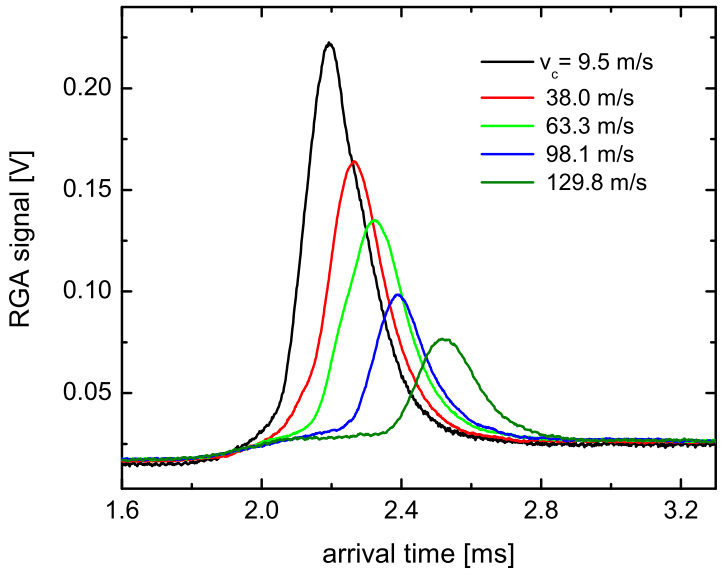

Figure 5.3: Signal of the reflected beam for different tip velocities. The gas source is again a 48:52 He:Ne mixture at 77 K. Shown is an average over 50 measurements each. The decreasing beam intensity with higher speed tips is partly due to a larger fanning effect and partly because the mirror reflectivity degraded over the time of the measurement. The broadening of the beam profile is a result of the averaging over 50 single measurements.

shot, due to the varying rotational speed of the rotor and therefore varying reflection positions. This results in a broader peak when averaging.

We then calculate the velocity of the reflected beam taking into account the different delays, different rotor positions at the time of reflection, uncertainty in the speed of the original beam, and uncertainty in the ionization region. The resulting plot of final beam speed vs. mirror speed is shown in figure 5.4. The red line is a least square fit to the data points with slope -1.84, the black line is the one predicted by theory with slope -2.

The theoretical prediction still lies well within the error bars of the measure-

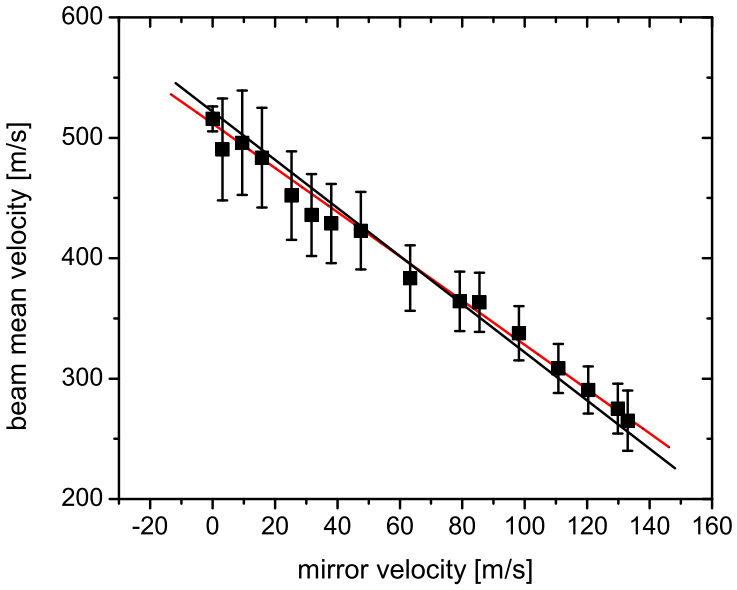

Figure 5.4: Beam velocity as a function of rotor tip or mirror velocity. The red line is the least sqare fit of the data, the black line is the theoretically expected dependence.

ment but it seems that there is a systematic deviation of the measurement from theory. During the analysis we tried using different values for the original beam velocity, various distances, rotor tip angles, angles at which the nozzle is triggered and other parameters. All resulted in either an offset of the points where the speed of the beam reflected from the standing rotor did not match the measured speed of the direct beam and/or a deviation from a linear dependence.

Since the distance between the point of reflection and the detector is very small in our current setup, the delay has a big influence on the calculated velocity of the final beam. If we systematically choose a wrong delay, the result might be the seen deviation from the theoretical curve. We hope to get a clearer picture of the problem when we put in the focusing mirror. The distance the slow beam travels

would be tripled, resulting in a much better time of flight analysis in which the influence of the delay would be much smaller.

5.3 Crystal life time

Previous research suggests that the crystal surface stays inert over several days [14] but in our experience the crystals deteriorate with a much faster rate. Figure 5.5 shows the intensity of the beam reflected from the standing rotor as a function of time. The data plotted in red was taken during a "normal" run where we measured the speed of the slow beam at different rotational velocities and stopped the rotor from time to time to record the reflection probability. The red curve is a least square fit of a double exponential decay; the two time constants are 2.5 min and 38.5 min which hints that two processes are responsible for the decrease of reflectivity.

It is well known that silicon loses its passivation in the presence of ion gauges. Electron and ion bombardment break the Si-H bond and the free space on the surface is occupied mainly by hydrocarbons present in the vacuum chamber. But hydrocarbons can also adsorb on the mirror surface without prior particle bombardment and an improvement of the vacuum should in principle improve the crystal lifetime.

A control measurement confirms our suspicions. The data plotted in black in figure 5.5 again shows the reflection probability over time, but this time the rotor remained stationary and the RGA was only turned on for a few seconds to measure the reflection probability, except for the time between data point 5 and 6 where it was left on for 40 minutes. Also, a cryogenic cold finger was placed on the 8 inch flange that is used to exchange crystals. It improved our vacuum drastically; within half an hour we had pumped the chamber from atmospheric pressure to 10^{-8}torr which normally takes at least one day. Within a few hours the pressure had dropped to 10^{-9}torr.

Surprisingly, the reflection probability not only decreased at a slower rate, it

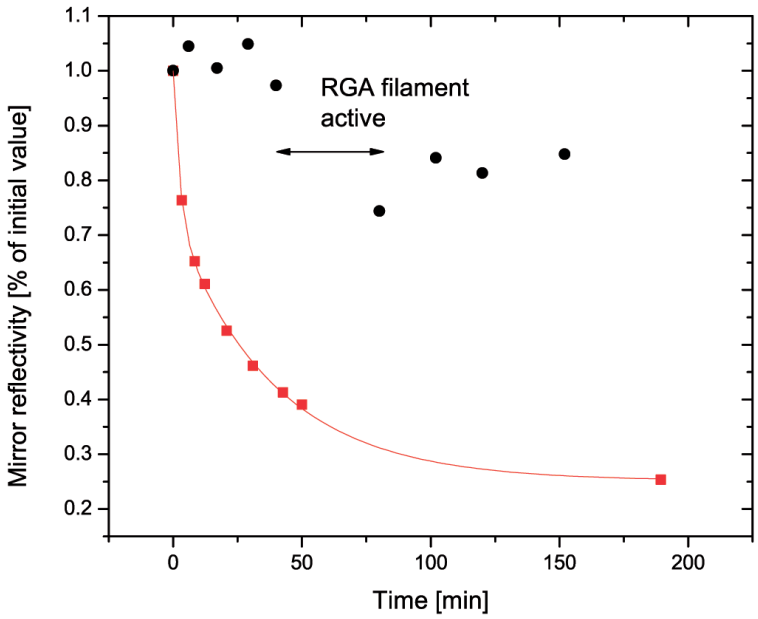

Figure 5.5: Mirror reflectivity over time. The red data points where taken in between and after the measurements for figure 5.3 with active RGA and no cold trap. The least sqare fit (red) shows a second order exponential decay with time constants 2.5min and 38.5min. The black data points were taken in a dedicated experiment with the filament only on during the data collection and a cold trap on the chamber.

stayed constant as long as the ionizer of the RGA was turned off. When the RGA was left on for 40 minutes, the reflection probability dropped to 74% percent of its original value but recovered again to 84%. The reason for the recovery might be that the crystal was first heated by the glowing filament of the RGA which decreased the Debye Waller factor. When it cooled down, the Debye Waller factor, and therefore the reflection probability, increased again. To explain the effect by temperature increase alone, however, the mirror would have needed to be heated to about 200°C.

The cold trap used for this experiment was borrowed and we are currently designing a custom cold trap for permanent usage.

Chapter 6

Future work

6.1 Improving the performance of the apparatus

As described in the above chapters we have demonstrated that slowing a supersonic beam by reflection of a moving rotor is in principle possible. However, the resulting beam does not yet have the desired properties we had hoped for when simulating the process.

One crucial step is to redesign the spindle holding the rotor to reduce its mass and drive the resonance frequencies of the shaft further up. Only faster rotation speeds of the rotor will result in a slower beam. Since only cryogenic helium produces a very intense and monochromatic beam, our ultimate goal would be to slow a pure helium beam to about 50 m/s which requires a rotation frequency of 130 Hz.

Without at least one additional mirror in the "mirror chamber", we will not be able to extract the beam and will not be able to use the focusing mirror to compensate the fanning effect. Also, we can only state reflection probabilities if we measure the direct and the reflected beam with the same RGA, which again requires at least one additional mirror. The gain of the two electron multipliers that are used in the two RGAs can easily differ by a factor of 10 because they might have

degraded with different rates and have been in use for different amounts of times. Even if we could calibrate the gain by measuring a background gas and comparing the two readings, the two RGAs would still be mounted in different geometries and we do not know what influence this has on the ionization probability.

Finally, atoms arriving at the focusing mirror can be tuned to have velocities below or above the diffraction threshold (299 m/s for (111)Si). Beams with higher atom velocities will be diffracted by the crystal surface; beams with lower velocities can only be reflected specularly. We should therefore see a rise in flux as soon as we tune the beam velocity from over 299 m/s to below that limit.

6.2 Velocity dispersion compensation piston

Our method of slowing lowers the beam's degree of monochromaticity because it does not change the standard deviation in translational velocity. This effect can be compensated for by taking advantage of almost perfect correlations between the velocity and the position of the atoms in the slow beam (see figure 3.4). Due to the short opening time of the nozzle and relatively slow propagation velocity, atoms with different velocities are spatially separated by the time of flight. The relationship between the velocity of an atom and its relative position in the beam can be used to compress the velocity of the atom pulse by reflecting the atoms from an accelerating mirror. Assume that the fastest atoms, which arrive at the mirror first, are reflected without having their velocity changed. The slower atoms will be given a kick in velocity upon reflection from the accelerating mirror. Thus, if we find a suitable acceleration, the correlation between an atom's longitudinal position in the beam and its velocity will allow us to accelerate each of the slower atoms up to the speed of the fastest atoms, thereby increasing the atomic beam's degree of monochromaticity.

In our simulation a 49 m/s $\pm$ 3 m/s atomic beam can be compressed to 55.3

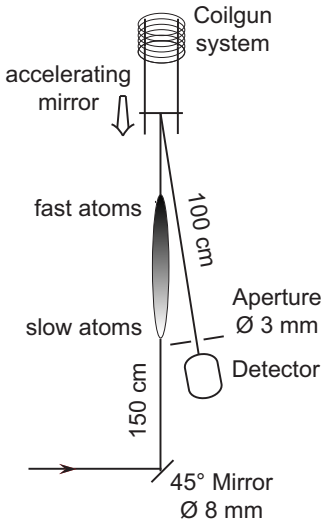

Figure 6.1: Schematic drawing of the proposed velocity compression piston. The atomic beam collides with an accelerating mirror which makes the beam more monochromatic. The mirror is accelerated by a coil gun setup.

m/s ± 0.2 m/s given a mirror that can be accelerated by about 60 g. One method of achieving such an acceleration is to mount the mirror on the projectile of a coil gun. A schematic drawing of a possible realization is shown in figure 6.1. Using this acceleration method, the acceleration of the mirror can be controlled by simply tuning the current in the coils. The puck can be decelerated and returned to its original position by a second "inverse" coil gun behind the accelerating coils. Coil guns capable of 5000 g accelerations [27] lead us to believe that an experimental realization of such a system is feasible.

6.3 Atom beam splitter

In previous atom optical systems, beam splitting has been accomplished by diffraction from microfabricated transmission gratings [2], diffraction from standing waves of light [28], and by momentum transfer due to atomic transitions [29]. In each of these systems, it is difficult to obtain large opening angles. For the diffraction based

beam splitters, the opening angle is determined by the ratio of the de Broglie wavelength of the atoms in the beam to the period of the grating used. By tuning the final velocity of the slow beam we can achieve atom de Broglie wavelengths in the range of 1-10 Å. A grating period on the order of the de Broglie wavelength would provide large opening angles and we believe that such a grating could be constructed from a single crystal surface. Utilizing the periodic structure of a crystalline lattice to create a reflection grating would give a grating period of the appropriate size, yielding the desired opening angles. By controlling the velocity and incident angle of the atoms, it should be possible to restrict diffraction to only a few open channels. As such, the flux in any one channel should be greatly enhanced. Furthermore, by tuning the incoming atom beam energy to match the energy of a selective absorption resonance it could be possible to enhance the atom flux into a particular diffraction order associated with that resonant state.

6.4 Proposed uses of the beam

A high flux, cold, low energy atom beam is well suited to several experimental applications. In particular, the slow beam would work well for studies of atom surface interactions and atom interferometry.

6.4.1 Characterizing the atom surface potential

One way to better characterize the atom surface potential would be to study the reflected intensity of an atom beam at different incident energies. Certain incident energies would couple with the bound resonant states of the atom-surface potential through diffraction channels. By measuring the incident energies that couple to these resonant states, one could determine the energy level structure, and thus the precise shape, of the atom-surface potential. There are two reasons our proposed beam would work so well for these studies. First, the energy resolution of 1.5

μeV as described in 3.4 would give us a much greater resolution than a standard supersonic beam. Second, the slow and tunable velocity of our atoms would allow us to study lower energy regimes than have previously been accessible. Finally, a precise measurement of the diffracted angle at a known velocity would provide an independent means by which to measure the lattice constant.

6.4.2 Atom interferometer

The predicted slow beam would provide many advantages when used for atom interferometric purposes. Ground state noble gases are insensitive to magnetic fields to first order, and due to their low polarizability they are approximately 100 times less sensitive to stray electric fields than the Alkali atoms. For a white light geometry Mach-Zehnder interferometer with length L, rotating at a rate Ω around an axis perpendicular to its plane, the phase shift is $\varphi = \frac{2\pi\Omega L^2}{vd}$, where d is the grating spacing and v is the velocity of the atoms [30]. Thus the sensitivity is inversely proportional to the velocity, favoring a slow beam. The phase shift for an acceleration a transverse to the direction of atomic motion is $\varphi = \frac{2\pi a L^2}{v^2 d}$ [30]. Here the phase shift is inversely proportional to the square of the velocity of the atoms. Since for many applications the sensitivity will be shot noise limited, the signal to noise ratio will scale with the square root of the number of atoms detected per unit time. For this reason, a high flux beam will give better counting statistics and thus a higher signal to noise ratio.

The relative phase shift of the atoms in the interferometer is inversely proportional to the grating spacing distance. As such, another method for increasing the sensitivity of the interferometer is to reduce the grating period. The single crystal reflection grating could provide a means for doing this. In particular, one could construct an atomic interferometer from a single crystal which would be an atomic analog to the perfect single crystal neutron interferometer [12, 30]. A schematic of

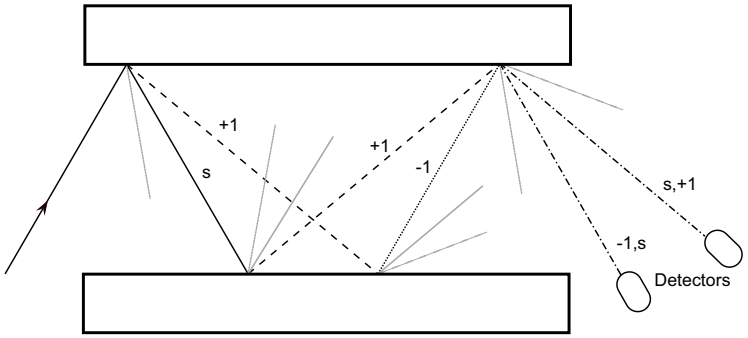

Figure 6.2: Schematic drawing of the proposed single crystal atomic interferometer. Specular reflected beams are labeled with an s, diffracted beams with the diffraction order.

a possible implementation of this can be seen in figure 6.2. With neutron interferometry the crystal acts as a transmission grating, while in our atomic analog crystal surface would act as a reflection grating. The advantages of this design are a large enclosed area, yielding increased sensitivity, high flux since diffraction is limited to only a few channels, and ease of alignment due to the monolithic design.

6.5 The magnetic slower

When we were thinking about ways to linearly decelerate or accelerate a silicon crystal, we considered moving a permanent magnet with an array of magnetic coils that would be switched on and off at the right moment, a coil gun. But if it is possible to manipulate a permanent magnet with a macroscopic magnetic dipole moment it should also be possible to decelerate atoms with an atomic dipole moment. Indeed, most elements and even some molecules (for example O_2) have a permanent dipole moment μ.

Slowing of atoms in pulsed magnetic fields makes use of the Zeeman effect and works analogue to the slowing of a Stark decelerator [31] which uses switched electrical fields. The energy of an atomic state with total angular momentum J and

magnetic quantum number m_J in a magnetic field of strength B shifts by

$$\Delta E = g m_J \mu_B B \tag{6.1}$$

where g is the Landé factor and $\mu_B = \frac{eh}{1 m_e c} = 9.3 \times 10^{-24} J/T$ is the Bohr magneton. Atoms in a state in which the product $g \cdot m_J$ is positive, gain energy with increasing magnetic field strength. Therefore, if a magnetic field gradient is present, these "low field seekers" are accelerated toward a region with low magnetic field to minimize their energy. Atoms in a state with $g \cdot m_J < 0$ on the other hand minimize their energy in regions with high magnetic field strength and are called "high field seekers".

A low field seeker flying toward a coil producing a magnetic field has to climb a magnetic hill because the magnetic field is strongest in the center of the coil. It loses kinetic energy and is slowed down during the approach. If the coil would be permanently magnetized, the atom will simply gain the same amount of kinetic energy it lost during the approach when it leaves the coil, and overall, its speed will not have changed. But if the coil is switched off in precisely the moment the atom passes through the center of the coil, the atom will not gain energy on the way out and will effectively be slowed. Similarly, a high field seeker can be slowed by switching the coil *on* shortly before the atom passes its center.

What sounds very simple in theory is experimentally not easy to realize. Very high magnetic fields (high currents) have to be switched within very short times. Several succeeding coils have to be employed if significant slowing is to be achieved. To slow down molecular oxygen with a magnetic dipole moment of 2 Bohr magnetons and a mass of 32 amu from 250 m/s to 150 m/s with 32 coils for example, each coil has to produce a magnetic field of several Tesla and must be switched within a few microseconds. Fortunately, the coil used in the supersonic valve to pull back the plunger was designed to deliver high magnetic fields for very short times. We are

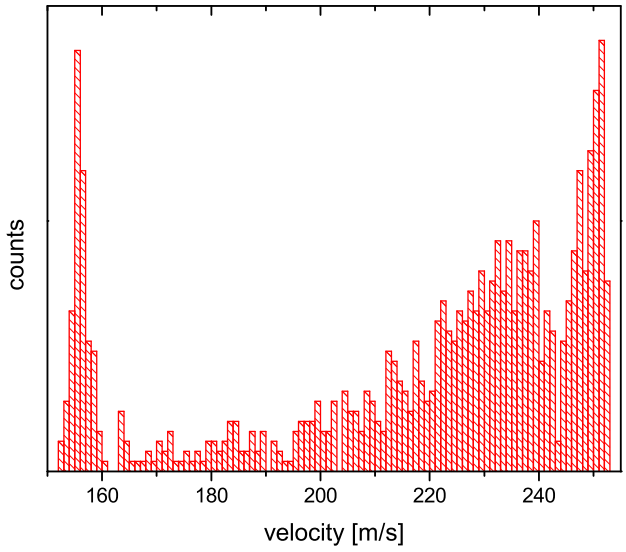

Figure 6.3: Simulation of magnetic slowing of O_2 with 32 coils from 245 m/s to 155 m/s. The coils are switched from 2 T to 0.2 T within 15 μs.

currently building similar coils, 6 mm long and with 30 windings, which produce a field of 2 T. We are also building the driver electronics to deliver the required 280 A per coil within 15 μs.

Figure 6.3 shows the simulated velocity distribution of oxygen in the low field seeking state, slowed with 32 coils as described above. For this simulation, the equation of motion is integrated for 1000 atoms with an initial velocity distribution around 250 m/s and a width of 30 m/s.

The narrow distribution of atoms around 155 m/s are the slow atoms we are aiming for; the remaining fast atoms will not be slowed because the timing of the coils is not matched to their initial velocity and the time they arrive at the magnetic slower which is located 0.5 m from the nozzle.

Chapter 7

Conclusions

The idea of slowing atoms by reflection from a moving crystal is intriguingly simple and has been around for a long time. Although there have been several attempts, to our knowledge, nobody has yet succeeded in realizing an experiment that produces a useful slow atom beam.

Our experiment differs in two major ways from previous attempts. First, we are using a cryogenic, pulsed valve. The pulsing increases monochromaticity and brightness of the beam and is ideally suited for the use with a rotor. Cryogenic operation decreases the velocity of the original beam. Second, the large diameter of our rotor allows relatively low rotation rates and decreases the spread and the related loss of flux of the reflected beam.

We showed that a high intensity beam of Helium with arbitrary low velocity can in principle be produced with our apparatus. We calculated the expected beam flux and the influence of a focusing mirror in the beam path. We also pointed out the correlation between velocity and arrival time of an atom at a specific point which can be used to scan a whole range of energies within a single shot.

Within the 4 months that have past since we received the vacuum chamber from our machine shop, we were able to slow a He:Ne mixture to less than half its

original speed without heating the beam and thus preserving its monochromaticity. Moreover, we are able to tune the wavelength of the reflected He atoms between 1.9Å and 2.5Å at will.

At the moment, a resonance of the shaft-spindle-rotor system is limiting our ability to spin faster and reach slower speeds. We are quite sure, however, that a new, lighter spindle will solve this problem and we are currently working on designing it. We are also planning to improve our vacuum by implementing a cold finger in the chamber and thus prolonging the lifetime of our atom mirrors. At the same time we are building a source for atomic hydrogen that will clean the surface and renew the passivation layer, thus regenerating the ability of the crystal to elastically reflect the beam.

Furthermore, to be able to extract a useful beam, we will have to place the focusing mirror in the chamber. Then we will also be able to give better estimates of the reflection probability of our crystals.

In this thesis we have shown a proof of principle with very promising results. Although there remains work to do before the predictions of the simulations are achieved, we feel confident that no fundamental limit will hinder us to reach lower beam velocities and higher fluxes which will ultimately lead to a versatile tool for precision measurements.

Bibliography

[1] *Atom Interferometry*, edited by P. Berman (Academic Press, San Diego, 1997).

[2] M.S. Chapman, C.R. Ekstrom, T.D. Hammond, R.A. Rubenstein, J. Schmiedmayer, S. Wehinger, and D.E. Pritchard, Phys. Rev. Lett. **74**, 4783 (1995).

[3] R. B. Doak, R. E. Grisenti, S. Rehbein, G. Schmahl, J. P. Toennies, and Ch. Wöll, Phys. Rev. Lett. **83**, 4229 (1999).

[4] *Atom and Molecular Beams: The State of the Art 2000*, edited by R. Campargue (Springer-Verlag, Berlin, 2001).

[5] D. Farías and K H Rieder, Rep. Prog. Phys. **61**, 1575 (1998).

[6] K. Burke, and W. Kohn, Phys. Rev. B **43**, 2477 (1991).

[7] R.B. Doak, K. Kevern, A. Chizmeshya, R. David, and G. Comsa, SPIE **2995**, 146 (1997).

[8] M. Gupta, and D. Herschbach, J. Phys. Chem. **105**, 1626 (2001).

[9] U. Even, J. Jortner, D. Noy, and N. Lavie, J. Chem. Phys. **112**, 8068 (2000).

[10] *Physics for Scientists and Engineers*, P. Tipler (W.H. Freeman/Worth Publishers, New York, 1999)

[11] H. Pauly, *Atom, molecule and cluster beams I: basic theory, production and detection of thermal energy beams*, (Springer-Verlag, Berlin, 2000).

[12] *Neutron Interferometry*, edited by U. Bonse and H. Rauch (Oxford Science Publications, Oxford, 1979).

[13] P. Dumas, Y.J. Chabal, and G.S. Higashi, J. Electron Spectrosc. Relat. Phenom. **54/55**, 103 (1990).

[14] D. Barredo, F. Calleja, A.E. Weeks, P. Nieto, J.J. Hinarejos, G. Laurent, A.L. Vazquez de Parga, D.A. MacLaren, D. Faras, W. Allison and R. Miranda, Surface Science, in press.

[15] J.R. Manson, Phys. Rev. B, **43**, 6924 (1991).

[16] D. MacLaren, Private Communication.

[17] B. Holst and W. Allison, Nature (London) **390**, 244 (1997).

[18] Stanford Research Systems Inc., www.thinksrs.com

[19] K. Kuhnke, K. Kern, R. David, and G. Comsa, Rev. Sci. Instrum. **65**, 3458 (1994).

[20] UGS Solid Edge, www.solidedge.com

[21] National Instruments LabView, www.ni.com

[22] Ferrotec, www.ferrotec.com

[23] Galil Motion Control Inc., www.galilmc.com

[24] Comsol Femlab, www.comsol.com

[25] Directed Light Inc., www.directedlight.com

[26] Manual SRS RGA 100/200.

[27] R.J. Kaye, E.C. Cnare,M. Cowan, B.W. Duggin, R.J. Lipinski,B.M. Marder, G.M. Douglas, and K.J. Shimp, IEEE Trans. on Magnetics **29**, 680 (1993).

[28] D.M. Giltner, R.W. McGowan, and S.A. Lee, Phys. Rev. Lett. **75**, 2638 (1995).

[29] M. Kasevich and S. Chu, Phys. Rev. Lett. **67**, 181 (1991).

[30] J.F. Clauser, Physica B **151**, 262 (1988).

[31] H. L. Bethlem, G. Berden, and G. Meijer, Phys. Rev. Lett. **83**, 1558 (1999).

Vita

Date of Birth:	October 5th 1982
Place of Birth:	Bad Kreuznach
Nationality:	German

Education

2005 - 2006	Studies of Physics at the University of Texas, Austin
2002 - 2005	Studies of Physics at the Julius-Maximilians-Universitt Wrzburg
2001 - 2002	Military Service (Wehrbereichskommando II)
1999 - 2001	Lina-Hilger-Gymnasium in Bad Kreuznach, 12th and 13th grade
1998 - 1999	Hunter-Huss-High School in North Carolina, USA (exchange student)
1992 - 1998	Lina-Hilger-Gymnasium in Bad Kreuznach, until grade 10
1988 - 1992	Elementary school in Freilaubersheim

Awards and Prizes

2005	C. Paul Boner Graduate Fellowship in Physics
2005	Full DAAD Fellowship
2003	Member of the e-Fellows Network (www.e-fellows.net)
2002	Formal appreciation of the Wehrbereichskommando II
2001	Prize of the DPG (German Physical Society) for outstanding performance in the subject Physics

Publications

Towards coherent control of supersonic beams: a new approach to atom optics A. Libson, M. Riedel, G. Bronshtein, E. Narevicius, U. Even and M. G. Raizen, New Journal of Physics **8**, 77 (2006) online on www.njp.org.

Elastic Slowing of a Supersonic Beam with an Atomic Paddle E. Narevicius, A. Libson, M. F. Riedel, C. G. Parthey, I. Chavez, U. Even and M. G. Raizen, submitted

Permanent Address: Haarbergweg 12
55546 Neu-Bamberg
Germany

This thesis was typeset with LaTeX 2_ε[1] by the author.

[1] LaTeX 2_ε is an extension of LaTeX. LaTeX is a collection of macros for TeX. TeX is a trademark of the American Mathematical Society. The macros used in formatting this thesis were written by Dinesh Das, Department of Computer Sciences, The University of Texas at Austin, and extended by Bert Kay, James A. Bednar, and Ayman El-Khashab.